



A single-ion-focused 393 nm laser for photon generation and qubit control

A master's thesis submitted to the faculty of mathematics, computer science
and physics, of the University of Innsbruck
in partial fulfillment of the requirements for the degree of

Master of Science (MSc)

carried out at the Institute of Experimental Physics under the supervision of
o.Univ.-Prof. Dr. Rainer Blatt,
Dr. Ben Lanyon

Presented by

Marco Canteri

Abstract

An ongoing project of building a three node quantum network is currently carried out at the university of Innsbruck with ion traps being the nodes of the network. To make entanglement between ions located in the three nodes, control over multiple ion-photon pairs is required. A laser beam has to focused down to a single ion to generate photons out of individual ions in a string. In this thesis, an optical system is designed and built for focusing and steering the laser beam responsible for the photon generation process. Our experiment traps $^{40}\text{Ca}^+$ ions, the 393 nm laser triggers the generation of a photon via a cavity enhanced Raman process. The photon is emitted in a cavity and leaks out from one side. The designed setup comprises of an AOD, for steering the beam in the microsecond timescale, a set of lenses for expansion and control of the laser beam, and a custom objective for focusing the light on the ions. The system was designed and simulated with the software Zemax, and ultimately built on top of the existing experiment. We report two experiments that demonstrate the capabilities of the newly built setup. The first experiment generated photons out of a single ion in a string without exciting the ions not involved in the process. In the second experiment we applied a phase gate on a single ion-qubit, the phase shift induced is measured with a Ramsey interferometer. In addition to demonstrate single qubit manipulation capability, this experiment also allowed for a measure of the focus spot: $1.2\text{-}1.3 \mu\text{m}$ with an upper bound on the addressing error of 10^{-3} . These experiments are a stepping stone towards the realization of the aforementioned quantum network, the next key experiment is already ongoing, photons are produced from different ions creating a photon train. Afterwards, entanglement between ion and photon has to be achieved for each ion-photon pair.

Contents

1	Introduction	1
2	Theoretical framework	5
2.1	Quantum logic with trapped ions	5
2.1.1	Quantum computer and quantum gates	5
2.1.2	Ion qubits and laser-ion interactions	7
2.1.2.1	Three-level model	11
2.1.2.2	Dissipative processes	12
2.2	Quantum networking with trapped ions	13
2.2.1	General introduction	13
2.2.2	Cavity QED	13
2.2.3	Photon generation	14
2.3	Basics of ion trapping	16
2.3.1	Linear Paul trap	16
2.3.2	Ion strings	17
2.3.3	Doppler cooling	18
2.4	Laser beam	20
2.4.1	Gaussian beams	20
2.4.2	Beam steering via Acousto-optical Deflectors	23
2.5	Experiments model	25
2.5.1	Addressed qubit manipulation	25
2.5.2	Addressed photon generation	27
3	Existing experimental system	29
3.1	Ion trap and key techniques	29
3.1.1	Calcium Ions	29
3.1.2	Trapping, cooling, and state readout	30
3.2	393 nm laser	33
3.3	Experiment control	34
4	Design and simulation of the addressing setup	37
4.1	Addressing system overview and requirements	37
4.2	Objective and AOD	40
4.3	Design simulation	40
4.4	Physical implementation	44
5	Experimental results	47
5.1	AOD	47

5.2	Full test setup characterization	48
5.2.1	Waist: Knife-Edge method	49
5.2.2	Waist: Camera	50
5.2.3	Polarization	51
5.2.4	Stability	52
5.3	Final installed system	54
5.3.1	Single qubit manipulation	54
5.3.2	Photon production	57
6	Conclusions and outlook	61
	References	62
	Appendix	65
A	AOD datasheet	65
B	Polarization characterization	69

Chapter 1

Introduction

A next step in technology advancement is represented by quantum technology, as it offers a radically new approach for the fields of computation, communication, simulation, and metrology [1]. For example, classical computers are limited in solving some particular problems that scale exponentially, and therefore a new approach is needed. Quantum computing can exploit particular features of quantum mechanics that have no classical counterparts, this allows for a speed up for a certain class of problems such as factorizing numbers [2], or searching in a database [3]. Moreover, simulating nature at its quantum level is a hard task for classical computer, while quantum computers are naturally prone to simulate quantum dynamics [4].

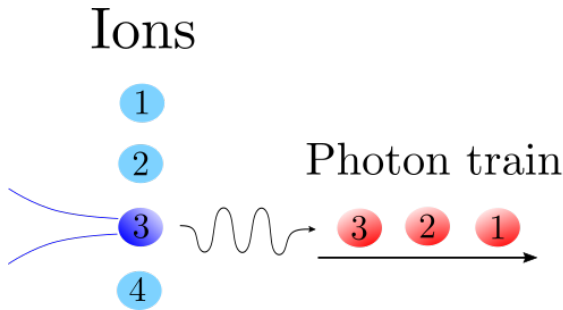
A collection of quantum computers interconnected via quantum channels forms a fully fledged quantum network [5]. However, for some quantum network applications, it is possible to relax the condition of having a universal quantum computer, a quantum device with a single qubit is enough as part of a functional quantum network with basic capabilities [6]. The concept of a quantum internet is to have a quantum channel along side with the classical channel, enabling the transmission of quantum information [6]. There are fundamental differences between a quantum channel and a classical link. Although the medium can be the same, such as optical fiber, a quantum channel must have additional abilities, such as distributing entanglement, or transmitting quantum states. Quantum networks have several applications: cryptographic wise they allow for more secure information transmission through Quantum Key Distribution [7], secure identification [8], blind quantum computation [9] and more [6]. Outside cryptography, quantum networks find applications in metrology: entanglement can be exploited to improve clock synchronization [10], and extend telescope's baselines [11]. Furthermore, quantum networks offer more efficient solutions to distributed system problems [12].

It is in this context that this thesis arises. Currently there is an ongoing project of building a three node quantum network between two buildings on the campus of the University of Innsbruck. The quantum nodes consist of ion traps: qubits are encoded in the electronic states of ions trapped in a Paul trap, while manipulation is done with laser pulses [13]. A 400 m optical fiber serves as link between the two buildings. This quantum network should have the ability to make entanglement with more than one other node in a network. This task requires the ability to connect multiple ions to multiple traveling direction-switchable photons. This is achieved with a single-ion-focused laser beam that can be used for photon generation. In this thesis, an optical system was designed and built for controlling the laser beam responsible for photon generation.

Photons are generated via a cavity enhanced Raman process [14], for which a 393 nm laser is used. When I started my master project, the 393 nm laser was shining on every ion in the trap. In this case, if an ion string were to be loaded, the light would couple to every ion and there would be no control over the single ion-photon pair. To get photons from individual ions in a string, this thesis presents the development of an optical system that focuses the 393 nm laser beam on a single ion, and has the ability to steer the beam on a timescale of a few microseconds, which is the typical time for photon generation operations and ion-qubit operations. The setup is per se not complex, but the design is critical. Ions separation is typically around 5 micrometers in our system, so the light should be focused down to $1 - 2 \mu\text{m}$, at the limits of the optical elements involved. The steering part is achieved with an acousto-optical deflector (AOD), which deflects the laser light on microsecond timescales proportionally to the applied input frequency allowing to control remotely the beam pointing of the system.

The AOD allows single ions in a string to be manipulated in two different ways:

SINGLE ION PHOTON GENERATION



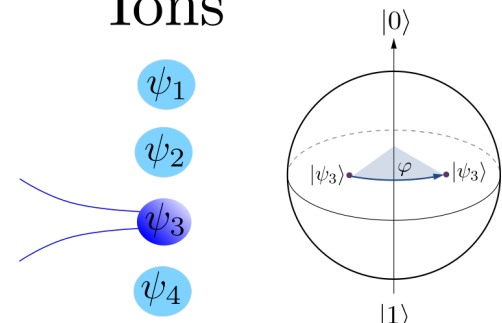
As illustrated in the sketch on the left, the idea is to generate photons from individual ions in a string. The laser beam is focused on a single ion, a laser pulse triggers the generation of a photon, the beam is then steered and focused on another ion to repeat the process. The approach we use is an ion-cavity system: the laser pulse triggers a cavity enhanced Raman process [14] that on resonance causes the emission

of a photon from one ion into the cavity. The photon subsequently leaks out from one of the cavity mirrors. In this thesis we set the goal of emitting photons from a particular ion without exciting any other ion in the string. This is a key step towards producing and controlling multiple photon-ion pairs.

SINGLE ION-QUBIT MANIPULATION

The same laser can perform quantum operations on the qubits encoded in the ions. Our goal is to manipulate the state of a single qubit without modifying the state of the others. Here the laser operates in a far-detuned regime, and induces an AC Stark shift on the $|0\rangle = |\text{S}_{j=1/2}, m_j = -1/2\rangle$ state of the ion-qubit implementing a phase gate [15]. In order to measure the AC Stark shift we perform a Ramsey interferometry experiment [16], where between the two $\pi/2$ pulses a detuned Stark pulse is introduced. This pulse shifts the relative phase of the qubit and therefore the amount of Stark shift can be inferred from the final qubit state.

Ions



The rest of this thesis is presented in the following way: Chapter 2 is devoted to the theoretical background necessary to understand the rest of the work. Here, the foundations

of quantum computing and networking are laid down, along with the basic concepts of ion trapping and Gaussian laser beams; Chapter 3 presents the existing experimental setup, i.e. the already built and working blocks of the experiment where the setup designed in this thesis has been added; Chapter 4 is the core of the thesis, here the final design made with the software Zemax and simulations of different aspects of the project are introduced and presented; Chapter 5 contains all the experimental results obtained. It is divided in two parts: first, the setup was built on an optical table, here we had the freedom to test different key properties of the performance of the system and decide whether or not it was satisfactory. After having the certainty that the system can work as desired, the setup was transferred and aligned on the main experiment where limited access did not allow for easy performance testing. Here, we carried out two experiments that demonstrate the capability of the built system: to manipulate single qubits and generate photons from single ions. The description and discussion of these results are in the second part of chapter 5. Lastly, in Chapter 6 a conclusion with a summary and a future outlook is given.

Chapter 2

Theoretical framework

Quantum computing is based on a general framework that does not depend on the physical platform. In this chapter, important concepts such as qubits, and quantum operations are described from a theoretical point of view, before showing how we can realize them with trapped ions. The same goes with quantum networking, the concept and the realization can be treated separately and they will be described in this chapter. Furthermore, in this chapter we will take a look into Gaussian beams and their properties. Since that is the shape emitted by laser, it is important to understand their characteristics and how to manipulate them. Lastly, Acousto-optical interactions are introduced and studied to give an idea of how AODs work and how they can be used to steer a laser beam.

2.1 Quantum logic with trapped ions

2.1.1 Quantum computer and quantum gates

The concepts of quantum computing are borrowed and extended from classical computational. In the classical case, information is mostly represented in terms of binary digits, the so called bit, essentially mapping information to a base-2 number. Information processing is done with gates acting on those numbers. The idea of a quantum computer is still to encode information in a binary form, but due to the nature of quantum mechanics, a quantum bit (in short qubit) gains new features that can be exploited to perform different kind of operations.

A qubit is formally a normalized wave function that can be written as a superposition of two orthogonal states indicated usually with $|0\rangle$ and $|1\rangle$:

$$|\psi\rangle = \alpha|0\rangle + \beta|1\rangle, \quad (2.1.1)$$

where α, β are probability amplitudes, i.e. two complex numbers that satisfy the relationship $|\alpha|^2 + |\beta|^2 = 1$. A qubit can be in any linear combination, i.e. α and β . The outcome of measuring a qubit will give the value 0 with a probability of $|\alpha|^2$ and 1 with a probability of $|\beta|^2$.

Qubits also have a geometrical representation that can be useful, equation (2.1.1) depends

on 4 real numbers, however since ψ is normalized, we can rewrite the expression as

$$|\psi\rangle = e^{i\gamma} \left(\cos \frac{\theta}{2} |0\rangle + e^{i\varphi} \sin \frac{\theta}{2} |1\rangle \right). \quad (2.1.2)$$

the global phase factor $e^{i\gamma}$ can be left out, as it does not influence the measurement outcome. This leaves us with only two real numbers: θ and φ . A qubit is therefore representable with only these two numbers that we can choose to represent geometrically with normalized spherical coordinates. The so called Bloch sphere is depicted in figure 2.1.1, every point on its surface represents a different state of the qubit. Here qubit manipulation can be visualized as trajectories on the surface. The drawback of this representation is that it is limited to only one qubit, so it loses usefulness when dealing with multiple qubits.

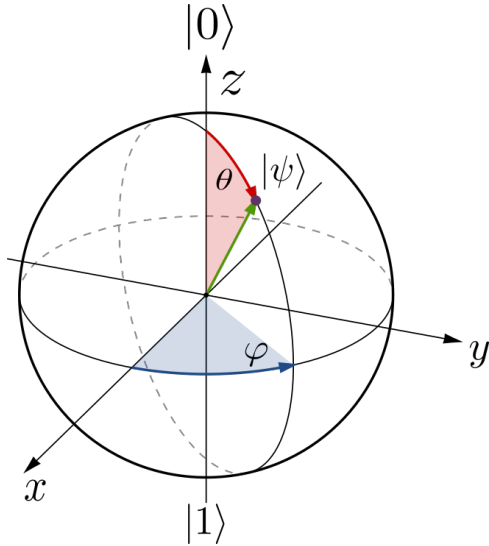


Figure 2.1.1: The Bloch sphere. The states $|0\rangle$ and $|1\rangle$ are at the poles of the sphere, every other point of the surface represents a superpositions of these states. A quantum gate can be seen as trajectory on the surface mapping one state to another.

An alternative way of dealing with qubits is via matrices. We can assign to the states $|0\rangle$ and $|1\rangle$ the following:

$$|0\rangle = \begin{pmatrix} 1 \\ 0 \end{pmatrix} \quad |1\rangle = \begin{pmatrix} 0 \\ 1 \end{pmatrix} \implies |\psi\rangle = \begin{pmatrix} \alpha \\ \beta \end{pmatrix}. \quad (2.1.3)$$

In this representation, rotations of qubits are calculated using 2×2 unitary matrices. These kind of operations are named *quantum gates* and they are the building blocks of quantum computing. Quantum algorithms can be written as a sequence of quantum gates and it is therefore important to understand them. For a single qubit, any gate can be written as combination of two operations [?]

$$U_z(\Theta) = \begin{pmatrix} e^{-i\frac{\Theta}{2}} & 0 \\ 0 & e^{i\frac{\Theta}{2}} \end{pmatrix} \quad U_\varphi(\theta) = \begin{pmatrix} \cos \frac{\theta}{2} & -ie^{-i\varphi} \sin \frac{\theta}{2} \\ -ie^{i\theta} \sin \frac{\theta}{2} & \cos \frac{\theta}{2} \end{pmatrix}. \quad (2.1.4)$$

These two matrices can be seen as two different rotations in the Bloch sphere, U_z is a

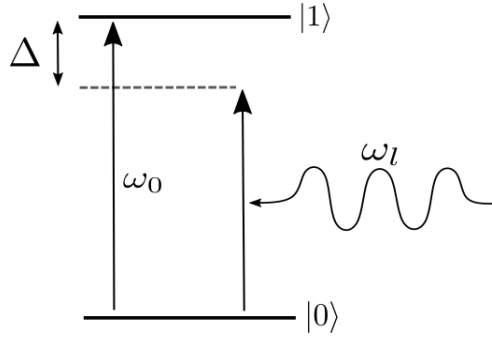


Figure 2.1.2: 2-level atom scheme, the ground and excited states are denoted as $|0\rangle$, and $|1\rangle$. ω_l is the laser frequency, which is detuned by $\Delta \equiv \omega_l - \omega_0$ from the transition frequency ω_0 .

rotation around the z axis by the amount Θ , while U_φ is a rotation on the $x - y$ plane around an axis tilted by φ . Important examples are the Hadamard gate H , which creates a superposition of one qubit starting from the state $|0\rangle$, or $|1\rangle$, and the phase shift gate R_ϕ that shifts the phase:

$$H = \frac{1}{\sqrt{2}} \begin{pmatrix} 1 & 1 \\ 1 & -1 \end{pmatrix} \quad R_\phi = \begin{pmatrix} 1 & 0 \\ 0 & e^{i\phi} \end{pmatrix}. \quad (2.1.5)$$

Gates that involve N qubits are written as $2^N \times 2^N$ unitary matrices, a famous example is the controlled not (CNOT) gate

$$\text{CNOT} = \begin{pmatrix} 1 & 0 & 0 & 0 \\ 0 & 1 & 0 & 0 \\ 0 & 0 & 0 & 1 \\ 0 & 0 & 1 & 0 \end{pmatrix}. \quad (2.1.6)$$

It can be shown [15] that the examples of this section: H gate, phase gate, and CNOT gate form a universal set of quantum gates, i.e. a sequence of these gates approximates every other quantum gate.

2.1.2 Ion qubits and laser-ion interactions

Qubits can be encoded in any pair of orthogonal states. In the case of an ion it is possible to take two internal electronic states, the qubit is then implemented in their transition. In figure 2.1.3 the level scheme of ${}^{40}\text{Ca}^+$ is presented. The lifetime of the excited level has to be long enough to carry out all the quantum operations without spontaneous scattering. A common choice is the transition $|\text{S}_{1/2}\rangle \rightarrow |\text{D}_{5/2}\rangle$, where the ground state $|\text{S}_{1/2}\rangle$ represents the state $|0\rangle$ and the excited state $|\text{D}_{5/2}\rangle$ will be $|1\rangle$. As these levels are separated by an optical frequency, this kind of qubit is often referred to as optical qubit. Lasers provide a way to directly manipulate the population of these two levels and therefore to manipulate the state of the qubit.

The interaction between ion and laser can be understood in terms of a simple model: a two-level atom with dipole interaction with the laser field. Consider the system in figure 2.1.2, where the states $|0\rangle$ and $|1\rangle$ are separated by a frequency ω_0 , while the laser is assumed to be monochromatic with frequency ω_l . The difference $\Delta = \omega_l - \omega_0$ is called

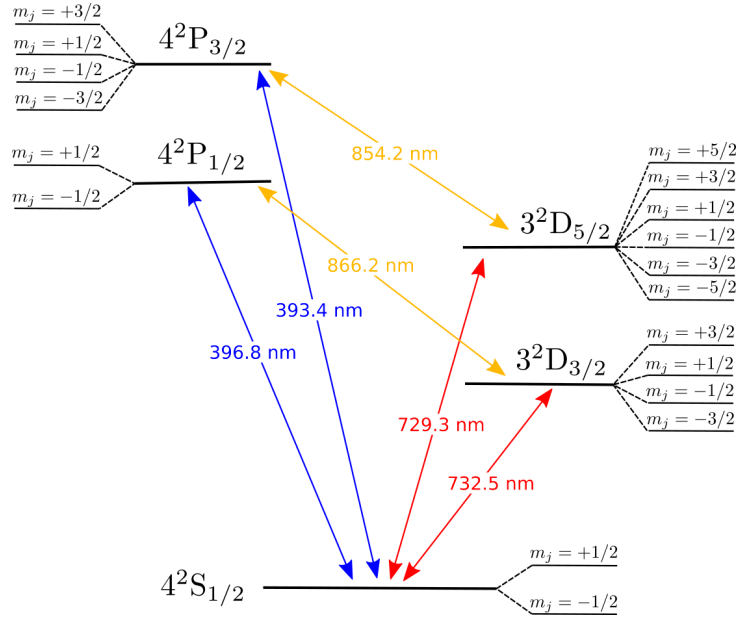


Figure 2.1.3: Level scheme of $^{40}\text{Ca}^+$. Detailed description is in section 3.1.1. For quantum computing purposes, the chosen qubit transition is the long lived quadrupole transition $|\text{S}_{1/2}\rangle \rightarrow |\text{D}_{5/2}\rangle$ at 729nm.

detuning and we assume to be in the near resonant regime $\Delta \ll \omega_0$. The laser light in this case can be described classically in the dipole approximation. This assumption can be explained as follow, the wavelength of transitions in an atom, are typically in the optical regime: hundreds of nanometers, which is order of magnitude greater than the typical atom dimension. Thus, the electric field can be considered constant over the atom size. This allows to expand the electric field in Taylor series and remove every spatial dependent term in the so called dipole approximation. The Hamiltonian of the atomic part can be written as:

$$H_a = \hbar\omega_0 |1\rangle\langle 1|, \quad (2.1.7)$$

where ω_0 is the frequency difference between the ground and excited state, the energy of the ground state has also been set to 0. The Hamiltonian of the interaction between the dipole atomic moment \mathbf{d} and the electric field of the laser can be written [?]

$$H_{int} = -\mathbf{d} \cdot \mathbf{E} \quad (2.1.8)$$

where the electric field will be treated classically and the dipole approximation is assumed. This means

$$\mathbf{E}(t) = \hat{\varepsilon} E_0 \cos(\omega t + \varphi) = \hat{\varepsilon} \frac{E_0}{2} (e^{-i(\omega t + \varphi)} + e^{i(\omega t + \varphi)}), \quad (2.1.9)$$

where $\hat{\varepsilon}$ is a the unit polarization vector. The next step is to work out the dipole operator, this can be done by applying the identity $|0\rangle\langle 0| + |1\rangle\langle 1|$ on both sides of d . Due to parity arguments [?], only the non diagonal terms are non vanishing, giving

$$d = \langle 0|d|1\rangle (|0\rangle\langle 1| + |1\rangle\langle 0|) \equiv \langle 0|d|1\rangle (\sigma + \sigma^\dagger). \quad (2.1.10)$$

Combining the last three equations yields

$$H_{int} = -\langle 0 | \hat{\epsilon} \mathbf{d} | 1 \rangle \frac{E_0}{2} (\sigma e^{i(\omega_l t + \varphi)} + \sigma^\dagger e^{-i(\omega_l t + \varphi)} + \sigma e^{-i(\omega_l t + \varphi)} + \sigma^\dagger e^{i(\omega_l t + \varphi)}) \quad (2.1.11)$$

A rotating wave approximation is used now, essentially σ (σ^\dagger) evolves under the Hamiltonian H_a in time as $\propto e^{-i\omega_0 t}$ ($\propto e^{i\omega_0 t}$), therefore we can drop the fast oscillating terms in the last equation and keeping only those that depend on time as $\propto e^{\pm i(\omega_l - \omega_0)t}$. The validity of this approximation is given by the fact that ω and ω_0 are in the optical regime, thus they oscillate extremely fast and average to zero, the interesting slow dynamic is given only by their difference, aka detuning. With this approximation we arrive at the final form of the interaction Hamiltonian

$$H_{int} = \frac{\hbar\Omega}{2} (\sigma e^{i(\omega_l t + \varphi)} + \sigma^\dagger e^{-i(\omega_l t + \varphi)}), \quad (2.1.12)$$

where we defined the Rabi frequency $\Omega \equiv -\langle 0 | \hat{\epsilon} \mathbf{d} | 1 \rangle E_0 / \hbar$. The Rabi frequency depends linearly with the applied electrical field and hence its square is proportional to the intensity of the laser $\Omega^2 \propto I$. To summarize, the final system Hamiltonian is

$$H = H_a + H_{int} = \hbar\omega_0 |1\rangle\langle 1| + \frac{\hbar\Omega}{2} (\sigma e^{i(\omega_l t + \varphi)} + \sigma^\dagger e^{-i(\omega_l t + \varphi)}). \quad (2.1.13)$$

This Hamiltonian depends explicitly on time, which could lead to unnecessary complications if we want to solve the dynamics. To eliminate the time dependence, we can go in the rotating frame with the unitary transformation $U = e^{i\omega_l t |1\rangle\langle 1|}$, the Hamiltonian in this frame is

$$\tilde{H} = -\hbar\Delta |1\rangle\langle 1| + \frac{\hbar\Omega}{2} (e^{i\varphi}\sigma + e^{-i\varphi}\sigma^\dagger) \quad (2.1.14)$$

The time dependence is now gone, and the unitary evolution matrix can be calculated as

$$U(t) = \exp \left\{ -\frac{i}{\hbar} \tilde{H}t \right\} = \begin{pmatrix} \cos \left(\frac{\tilde{\Omega}t}{2} \right) + i \frac{\Delta}{\tilde{\Omega}} \sin \left(\frac{\tilde{\Omega}t}{2} \right) & -ie^{i\varphi} \frac{\tilde{\Omega}}{2} \sin \left(\frac{\tilde{\Omega}t}{2} \right) \\ -ie^{-i\varphi} \frac{\tilde{\Omega}}{2} \sin \left(\frac{\tilde{\Omega}t}{2} \right) & \cos \left(\frac{\tilde{\Omega}t}{2} \right) - i \frac{\Delta}{\tilde{\Omega}} \sin \left(\frac{\tilde{\Omega}t}{2} \right) \end{pmatrix}. \quad (2.1.15)$$

Where $\tilde{\Omega} = \sqrt{\Delta^2 + \Omega^2}$ is the generalized Rabi frequency. With this matrix we can calculate all the dynamic we need. In the case of zero detuning $\Delta = 0$, we also notice that the matrix is the same as equation (2.1.4). Thus, a resonant laser pulse implements the qubit rotation $U_\varphi(\theta)$, the rotation around the z axis is performed with a laser pulse as well, but far detuned from the transition. We will explore this possibility later in the AC Stark shift.

As an example, let us take the atom in the ground state $|\psi\rangle = |0\rangle$ and apply the unitary evolution (2.1.15). The probability to be in the excited state becomes

$$\mathbb{P}\{|1\rangle\}(t) = |\langle 1 | U(t) | 0 \rangle|^2 = \frac{\Omega^2}{\Omega^2 + \Delta^2} \sin^2 \left(\frac{\tilde{\Omega}t}{2} \right) \quad (2.1.16)$$

This equation is plotted in figure 2.1.4. For $\Delta = 0$, we get a cosine behaviour, the so called Rabi oscillations. The probability amplitude for the electron, under continuous drive by a laser, will oscillate between the ground and excited state at a frequency Ω . Detuning damps the amplitude of such oscillations and increases the oscillation frequency. Rabi

oscillations are an important tool in quantum information, laser pulses can prepare the state of the qubit in any superposition, e.g. starting in the $|0\rangle$ state, a $\pi/2$ pulse ($\Omega t = \pi/2$ and phase $\varphi = 0$) will result in the state $(|0\rangle - i|1\rangle)/\sqrt{2}$, with a π pulse ($\Omega t = \pi$, $\varphi = \pi$) the population is completely transferred to another level $|0\rangle \rightarrow |1\rangle$. These pulses can be used to implement the Hadamard gate of equation (2.1.5).

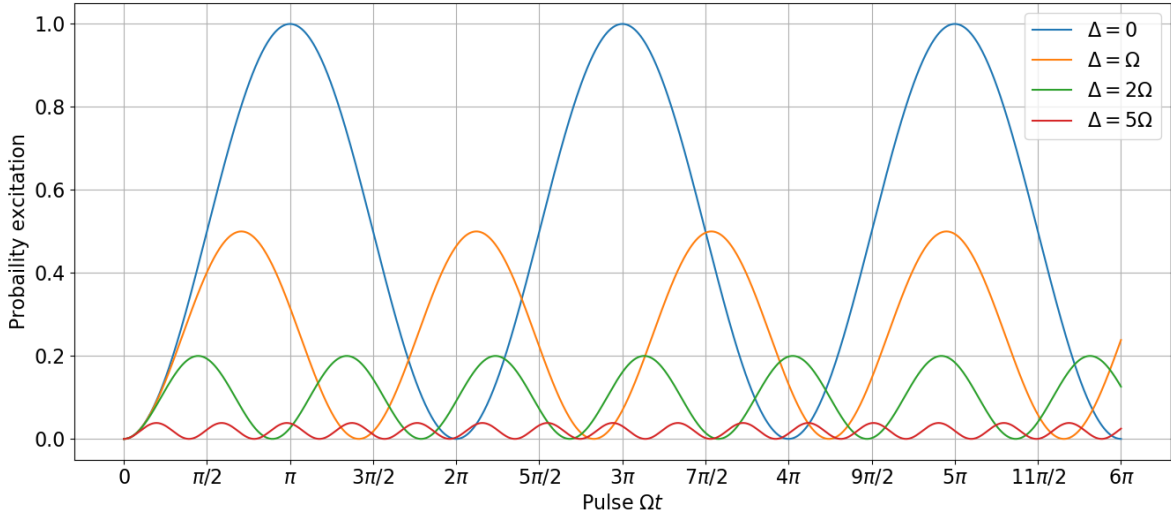


Figure 2.1.4: Rabi flops for different detunings Δ , starting from the $|0\rangle$ state.

As the light is detuned from the transition, Rabi oscillations are suppressed: the amplitude is reduced by a factor of 0.5 already with $\Delta = \Omega$, while a factor of 10 in reduction is achieved with a detuning of $\Delta/\Omega = 5$. However, another effect persists in the off-resonant regime, the energy levels are shifted. The shift δ can be calculated by finding the eigenvalues of the Hamiltonian (2.1.14), which can be written in matrix form and diagonalized. We find that there are two eigenstates $|+\rangle$ and $|-\rangle$ called dressed states with eigenvalues

$$E_{\pm} = -\frac{\hbar\Delta}{2} \pm \frac{\hbar}{2}\sqrt{\Delta^2 + \Omega^2}. \quad (2.1.17)$$

In the limit $\Delta \gg \Omega$, dressed states tend to the bare states $|+\rangle \rightarrow |1\rangle, |-\rangle \rightarrow |0\rangle$, and the energies becomes

$$E_{\pm} \rightarrow -\frac{\hbar\Omega}{2} \pm \frac{\hbar\Omega}{2} \pm \frac{\hbar\Omega^2}{4\Delta} \implies \delta = \pm \frac{\Omega^2}{4\Delta}. \quad (2.1.18)$$

The effective Hamiltonian for the off-resonant regime can be derived following a Markovian approximation [?]

$$H_{AC} = \frac{1}{\hbar\Delta} [\sigma, \sigma^\dagger] = \frac{\hbar\delta}{2} \sigma_z \quad (2.1.19)$$

The corresponding evolution is

$$U(t) = \exp \left\{ -\frac{i}{\hbar} H_{AC} t \right\} = \begin{pmatrix} \exp \left\{ i \frac{\delta}{2} t \right\} & 0 \\ 0 & \exp \left\{ i \frac{\delta}{2} t \right\} \end{pmatrix}. \quad (2.1.20)$$

This matrix implements the quantum gate from equation (2.1.4). Furthermore, AC Stark shift can also implement the phase gate R_ϕ of equation (2.1.5), but it requires a third energy level.



Figure 2.1.5: 3 level atom model. Two long lived ground states $|g_1\rangle$, $|g_2\rangle$ couple to an excited level $|e\rangle$ through two lasers of frequencies ω_1 , ω_2 detuned respectively Δ_1 , Δ_2 from the transitions.

2.1.2.1 Three-level model

We extend our model to a 3 level Λ type atom driven by two lasers, which closer resemble the real experimental situation. The model contains new effects that explain photon generation and qubit gates. In particular, stimulated Raman transition will be discussed, and we will show how, under certain conditions, the system can be approximated as an effective 2 level atom. The system is depicted in figure 2.1.5, two ground states $|g_1\rangle$ and $|g_2\rangle$ are present together with a common excited state $|e\rangle$. Two different lasers ω_1 , ω_2 drive the transition $|g_1\rangle \rightarrow |e\rangle$ and $|g_2\rangle \rightarrow |e\rangle$ with detunings $\Delta_1 = \omega_1 - \omega_{01}$ and $\Delta_2 = \omega_2 - \omega_{02}$. In the case of calcium, the ground states are $|S_{1/2}\rangle$, and $|D_{5/2}\rangle$. This is the qubit transition, and it is long lived, such that any spontaneous emission between S and D can be neglected. The excited level is $|P_{3/2}\rangle$ which can decay into both ground states.

In this model we assume that the two ground states are not separated by an optical frequency $\omega_{02} - \omega_{01} \ll \omega_1, \omega_2$, and that the detunings are nearly equal $\Delta_1 \simeq \Delta_2$. As a consequence, each laser light couples only to one transition.

The mathematical description is similar to the one described in section 2.1.2 for the 2 level atom with the addition of extra terms. Following the approach of [?], the bare atom Hamiltonian is

$$H_a = -\hbar\omega_{01} |g_1\rangle \langle g_1| - \hbar\omega_{02} |g_2\rangle \langle g_2|, \quad (2.1.21)$$

with the convention of setting the excited level energy to 0. The electric field is now the sum of the two lasers lights

$$E(t) = \hat{\varepsilon}_{01} E_{01} \cos(\omega_1 t \varphi_1) + \hat{\varepsilon}_{02} E_{02} \cos(\omega_2 t + \varphi_2). \quad (2.1.22)$$

We still apply the dipole and the rotating wave approximation to the interaction between electric field and atom. Finally transforming into the rotating frame gives the full final Hamiltonian as

$$H = \hbar\Delta_1 |g_1\rangle \langle g_1| + \hbar\Delta_2 |g_2\rangle \langle g_2| + \frac{\hbar\Omega_1}{2} \left(\sigma_1 e^{i\varphi_1} + \sigma_1^\dagger e^{i\varphi_1} \right) + \frac{\hbar\Omega_2}{2} \left(\sigma_2 e^{i\varphi_2} + \sigma_2^\dagger e^{i\varphi_2} \right), \quad (2.1.23)$$

where $\Omega_i = -\frac{\langle g_i | \varepsilon_i \cdot \mathbf{d} | e \rangle E_i}{\hbar}$, and $\sigma_i = |g_i\rangle \langle e|$. This Hamiltonian describes a Raman process, state population can be transferred coherently from g_1 to g_2 , without exciting the $|e\rangle$ level.

This happens at the Raman resonance $\Delta_1 = \Delta_2 \equiv \Delta$ if the detuning is large enough to eliminate adiabatically population in the $|e\rangle$ level, i.e. $\Delta \gg \Omega_1, \Omega_2$. Intuitively, this corresponds to the situation where the difference of the two driving frequencies ($\omega_1 - \omega_2$) is equal to the frequency splitting between $|g_1\rangle$, and $|g_2\rangle$.

As the excited level is eliminated, it can be shown [?] that the dynamics can be described as an effective 2 level system equivalent of that described in section 2.1.2. The effective Rabi frequency of the coherent population transfer $|g_1\rangle \rightarrow |g_2\rangle$ is [?]

$$\Omega_{eff} = \frac{\Omega_1 \Omega_2}{2\Delta}. \quad (2.1.24)$$

2.1.2.2 Dissipative processes

In the previous treatments we neglected dissipative processes as spontaneous emission to simplify the mathematical description. However, dissipative processes can play a role and it is important to understand them. Dissipative processes do not follow a Hermitian evolution, hence their mathematical description is done heuristically by adding terms in the Heisenberg equation

$$\frac{d\rho}{dt} = \frac{1}{i\hbar}[H, \rho] + \mathcal{L}(\rho). \quad (2.1.25)$$

This equation is usually referred to as master equation in Lindblad form, where ρ is the density matrix of the system. The superoperator $\mathcal{L}(\rho)$ contains phenomena not included in the Hamiltonian. For spontaneous emission, the form of $\mathcal{L}(\rho)$ is [?]

$$\mathcal{L}(\rho) = \frac{\Gamma}{2}(2\sigma\rho\sigma^\dagger - \sigma^\dagger\sigma\rho - \rho\sigma^\dagger\sigma), \quad (2.1.26)$$

where Γ is the decay rate. Γ represents the coupling between atom and environment, and can be calculated from Fermi's golden rule [?]

$$\Gamma = \frac{\omega_0^3|d|^2}{3\pi\varepsilon_0\hbar c^3}. \quad (2.1.27)$$

The master equation (2.1.25) can be explicitly written for every component of the density matrix ρ , in the rotating frame they are called optical Bloch equations. The solution for the excited population in the case of the 2 level atoms shows that the effect of spontaneous emission is to damp Rabi oscillations. In this case, on long time scale population exchange is suppressed, as it reaches a steady state. This regime is presented in section 2.3.3.

In the case of the three level model, the excited level $|e\rangle$ can decay to both ground states with rates Γ_{g_1} , and Γ_{g_2} . We are most interested in the decay rate $\Gamma_{g_1} \equiv \Gamma$ from $|e\rangle \rightarrow |g_1\rangle$ as the other transition in calcium is often repumped. In this case, in the effective 2 level system picture, the spontaneous emission is modified as [?]

$$\Gamma_{eff} = \left(\frac{\Omega_1}{2\Delta_1} \right)^2 \cdot \Gamma. \quad (2.1.28)$$

The ratio between this result and the AC Stark shift (2.1.18) $\delta/\Gamma_{eff} \propto \Delta$ dictates which effect is dominant, i.e. by detuning properly, spontaneous scattering can be eliminated leaving only Stark shift as effect. This regime can be used to implement a phase gate where the qubit is encoded in the $|g_1\rangle \rightarrow |g_2\rangle$ transition and the phase of $|g_1\rangle$ is manipulated by

Stark shifting the transition $|g_1\rangle \rightarrow |e\rangle$. In the experiment of section 5.3.1, we implement this gate on a single ion in a string.

2.2 Quantum networking with trapped ions

2.2.1 General introduction

A quantum network is a collection of quantum processors, denominated nodes, interconnected with quantum channels. Quantum channels have the unique property to be able to transmit quantum state among the nodes and distribute entanglement over the network [5]. There are two classes of quantum networks which are differentiated by the purpose, networks can be used for transmission of information, i.e. communication, or for distributed quantum computation, i.e. scaling of quantum processors [?]. In these two cases the topology of the network is different, but the core elements are the same: a node, where quantum information is prepared, manipulated, and stored; and a link that connects nodes. Links can be realized in free space [?] or with optical fibers, photons can carry quantum information over long distance with high speed. Nodes can be realized using different physical systems: trapped ions [?], neutral atoms [?], atomic ensembles [5]. Nodes and links are connected through an interface that converts a stationary qubit in a node to a flying qubit over the network. In the next section we will explore how an interface can be realized by placing an ion based quantum memory in an optical cavity. For a fully deployed quantum network, many challenges have to be faced. Faithful transmission of a quantum states over long distances can be a daunting problem as quantum information cannot be cloned [?], and noisy channels can destroy the delicate nature of qubits. Quantum repeaters have been designed [?] to circumvent these problems through a series of protocols which include error correction, or entanglement purification [?]. More protocols are also available to entangle qubits located in spatially separated quantum nodes [?]. Once entanglement has been established between nodes, other network functionalities become available, like for instance teleportation [?]. Entanglement generation, and quantum repeaters are just some examples of the fundamental steps necessary for building a quantum network, for a more in depth review look at [6].

2.2.2 Cavity QED

Trapped ion can generate photons and therefore be used as quantum nodes in a quantum network. The process of photon generation is based on cavity QED (cQED) and therefore we give here a small introduction. A cavity placed around ions has the purpose to improve the efficiency of photon collection as the probability of a photon to be emitted in the cavity mode is greatly enhanced with respect to emitting in free space [?]. Additionally, it allows for a better control of the photon waveform [?].

In this section we describe a simple model of a two-level system in a cavity following the approach of [?]. We described the cavity electric field as quantized, with a, a^\dagger the creation and annihilation operators of a single photon in the cavity mode. The quantized electric field assume the form of

$$E = A(f(r)a + f^*(r)a^\dagger) \quad (2.2.1)$$

where A is an amplitude, and $f(r)$ is the spatial mode profile. The interaction between the field and the cavity is

$$H_{int} = -d \cdot E = \hbar g(\sigma a^\dagger + \sigma^\dagger a), \quad (2.2.2)$$

where $g = A \langle 0|d|1\rangle f(r)$ is called cavity coupling constant. It is analogous to the Rabi frequency, it gives an idea of the coupling between the cavity field and the 2-level atom. An important dependence of g can be found by considering that $f(r)$ is inversely proportional to the volume of the cavity V , i.e.

$$g \propto \langle 0|d|1\rangle \sqrt{\frac{\omega}{2\varepsilon_0 \hbar V}}. \quad (2.2.3)$$

The coupling therefore, increases with decreasing cavity volume and viceversa. The total system Hamiltonian includes also the atomic part, and a single mode optical field, it takes the name of Jaynes-Cummings Hamiltonian and it is written as [?]

$$H = \hbar\omega_0 |1\rangle\langle 1| + \hbar\omega a^\dagger a + \hbar g(\sigma a^\dagger + \sigma^\dagger a). \quad (2.2.4)$$

The presence of a cavity makes dynamics more interesting, especially when considering spontaneous emission and interaction with cavity modes. For a mathematical description the master equation (2.1.25) is used. In our case, we are most interested in two processes: spontaneous emission in a free space field mode, and decay in one cavity mode and out of the cavity. The first is quantified with the decay rate $\Gamma = 2\gamma$, while the latter is characterized by the decay rate κ (half width half maximum). The decay rate κ depends exclusively on the cavity parameters as [?]

$$\kappa = \frac{c\pi}{FL}, \quad (2.2.5)$$

where F is the cavity finesse, and L the length. g, κ, γ are the most relevant experiment parameters in cQED. In our experiment the designed cavity is near concentric with a length of $L = 19.9$ mm. The maximum g factor achievable with this geometry is $g_{max} = 2\pi \times 1.53$ MHz, while the decay rate is $\kappa = 2\pi \times 70$ kHz. More information on our cavity can be found in [?] and in the upcoming thesis of J. Schupp.

2.2.3 Photon generation

Photons are generated from the ion via cavity-mediated Raman transition (CMRT). The CMRT can be explained using the three-level atom scheme, in figure 2.2.1 the relevant calcium levels for the Raman process are displayed. The electronic states are shifted due to a magnetic field generated by a permanent magnet perpendicular to the cavity axis and at 45° with respect to the trap axis. In the experiments we start from the state $|S_{1/2}, m_j = -1/2\rangle$, from here three choices of polarization can be taken: σ^-, π, σ^+ , for each choice three Raman transitions are possible. We can choose for instance

$$|S_{1/2}, -1/2\rangle \rightarrow |P_{3/2}, -3/2\rangle \rightarrow |D_{5/2}, -5/2\rangle. \quad (2.2.6)$$

In this case the transitions strengths, i.e. the projection of the laser polarization onto the dipole moment, and the same projection onto the cavity axis are maximized [14]. The

qubit is encoded in the $|S_{1/2}, -\frac{1}{2}\rangle \rightarrow |D_{5/2}, -\frac{5}{2}\rangle$ transition. CMRT is a coherent process similar to the Raman one described in section 2.1.2.1. A single laser pulse with strength Ω couples the $S_{1/2}$ level to the $P_{3/2}$ level, which is coupled to the $D_{5/2}$ via the cavity. Therefore, the electron state is transferred from the state $|S_{1/2}\rangle \rightarrow |D_{5/2}\rangle$ by absorbing a laser photon and emitting a cavity photon. The final state is therefore $|D_{5/2}\rangle |1\rangle$, where $|1\rangle$ indicates one photon in the cavity. Afterwards the photon leaves the cavity leaving the system in the $|D_{5/2}\rangle |0\rangle$ state. The difference with the Raman process is that instead of two lasers, the CMRT is driven by one laser and by the cavity standing electric field. As such, the effective Rabi frequency (2.1.24) of the population transfer is modified as [?]

$$\Omega_{eff} = \frac{\Omega g}{\Delta}, \quad (2.2.7)$$

where the Rabi frequency of the second laser is now replaced by the atom cavity coupling g . Furthermore, in the CMRT a photon is emitted in the cavity mode. The Raman resonance appears when the detuning Δ of the laser and the cavity are the same, moreover the detuning is chosen such that spontaneous emission from the $P_{3/2}$ state is eliminated. The effective spontaneous decay rate from this level is from equation (2.1.28)

$$\Gamma_{eff} = \left(\frac{\Omega}{2\Delta} \right)^2 \Gamma \quad (2.2.8)$$

The effective Rabi frequency Ω_{eff} and the effective spontaneous decay Γ_{eff} are competitive effects and the ratio of the two depends on the detuning $\Omega_{eff}/\Gamma_{eff} \propto \Delta/\Omega$. It is therefore possible to eliminate spontaneous emission effects if the detuning is large enough.

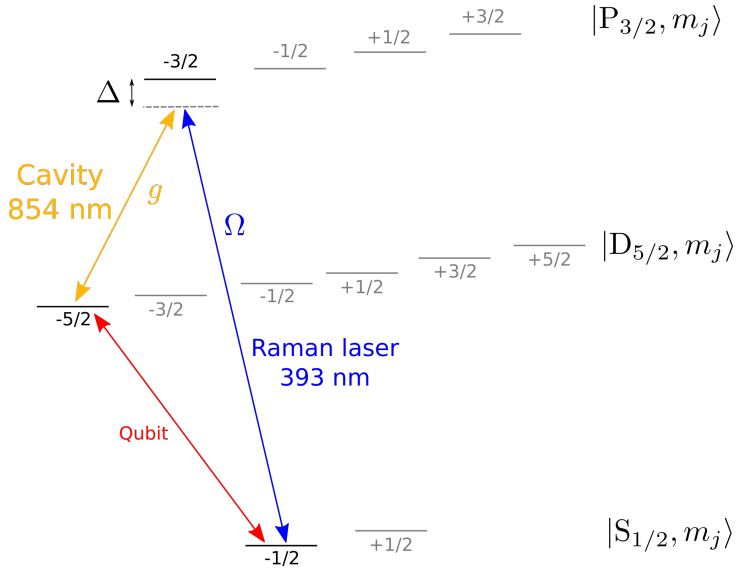


Figure 2.2.1: Displayed is the Zeeman structure of the relevant manifolds of calcium for the cavity-mediated Raman process. Here only one choice for the Zeeman level is depicted, but other are also possible. If the cavity and the Raman laser have the same detuning Δ , an electron in the ground state $|S_{1/2}\rangle$ absorbs a 393 nm photon and ends in the $|D_{5/2}\rangle$ state after emitting a 854 nm photon in the cavity.

Typical numbers are $\Omega = 2\pi \times 40$ MHz, detuning $\Delta = 2\pi \times 400$ MHz, $g = 2\pi \times 1$ MHz, and from table 3.1.1, $\Gamma = 2\pi \times 21.4$ MHz. With these conditions we have $\Omega_{eff} \sim 628$ kHz

$> \Gamma_{eff} \sim 336$ kHz. The regime we work in is thus $2\kappa > \Omega_{eff} > \Gamma_{eff}$. In our experiment, CMRT is used to produce photons from ions in the trap. The experiment in section 5.3.2 makes use of it by generating photons from a single ion in a string.

2.3 Basics of ion trapping

2.3.1 Linear Paul trap

Ions are particles that carry an electric charge, therefore electric fields can be used to control ions and trap them. In order to achieve confinement in 3 dimensions, a 3D potential $\phi(x, y, z)$ with minima in all directions is needed. However, it follows directly from Maxwell equation $\nabla^2 \phi = 0$ that the potential must be antitrapping at least in one direction. There are two workarounds for this problem: the first one introduces magnetic fields to trap particles in some directions, this takes the name of Penning trap [?]. The second solution is the so called Paul trap, and it is what we are going to describe in this section. The idea is to introduce a time varying potential, such that the antitrapping direction is constantly switching between two different dimensions. The particles will therefore experience an effective confinement in all directions if the switching is fast compared to the time it takes the particle to respond.

The shape of the trap can be adapted to load more ions in different geometries. In our work we utilize a linear Paul trap, which is elongated in one direction. The confinement in this direction is weaker and thus loaded ions will align in a single long string. This kind of trap is depicted in figure 2.3.1.

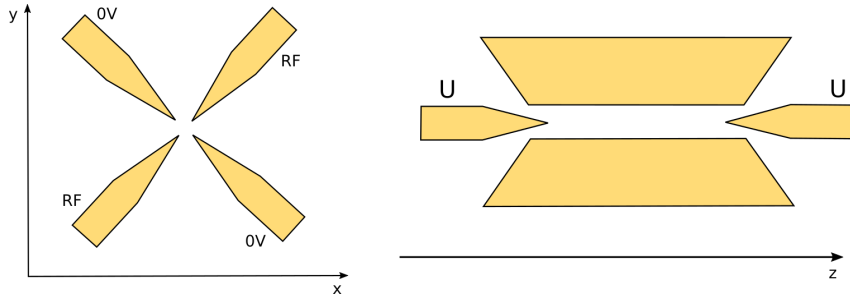


Figure 2.3.1: A linear paul trap. U is the voltage applied to the electrodes trapping in the z direction, while in the $x - y$ plane trapping is achieved with a radio frequency signal.

The confinement in the $x - y$ plane is provided by 4 electrodes, two of which are grounded and the other two are connected to a radio frequency source. This design is similar to a mass filter, with the difference of additional endcaps electrodes in the z direction that plug the trap and confine also in the axial direction.

The potential inside the trap can be described for the $x - y$ plan independently from the z direction. In the case of a linear Paul trap the radial potential is [?]:

$$\phi = \frac{\Phi_0}{2r_0^2} (x^2 - y^2), \quad (2.3.1)$$

where r_0 is the distance from the center of the trap to the electrodes. The amplitude consists of a static part U_0 and a dynamical one $\Phi_0 = U_0 + V \cos(\Omega_{RFT})$. The study of

the particle's motion with mass m and charge e inside the trap can be done with classical physics, Newton's second law in this case is

$$m\ddot{x} = -q\frac{\partial\phi}{\partial x} = -\frac{ex}{r_0^2} (U_0 + V \cos(\Omega_{RF}t)), \quad (2.3.2)$$

and similarly for \ddot{y} . This equation can be written in the form of Mathieu equation [?] by defining two parameters:

$$a_x = \frac{4eU_0}{\Omega_{RF}^2 r_0^2 m}, \quad q_x = \frac{2eV}{\Omega_{RF}^2 r_0^2 m} \implies \ddot{x} + \frac{\Omega_{RF}}{4} (a_x + 2q_x \cos(\Omega_{RF}t)) x = 0 \quad (2.3.3)$$

and with a change of variable $\tau = \frac{\Omega_{RF}t}{2}$ we end up with

$$\frac{\partial^2 x}{\partial \tau^2} + (a_x + 2q_x \cos(2\tau)) x = 0 \quad (2.3.4)$$

This kind of equations have stable solutions that can be found in a recursive way with Floquet theorem [?]. In the limit $a_x \ll q_x \ll 1$, solutions to (2.3.4) are found to be

$$x(t) = x_0 \cos(\omega_x t + \phi_x) \left[1 + \frac{q_x}{2} \cos(\Omega_{RF}t) \right]. \quad (2.3.5)$$

Here, we recognize a slowly varying oscillation ω_x , referred to as *secular motion*, with amplitude modulated by a faster oscillation Ω_{RF} , called *micromotion*. The approximation, named secular, is valid only in the case $\omega_x \ll \Omega_{RF}$. The frequency ω_x is given in the solution as

$$\omega_x = \frac{\Omega_{RF}}{2} \sqrt{a_x + \frac{q_x^2}{2}}. \quad (2.3.6)$$

By imposing real solutions to (2.3.6), the stability diagram of the trap can be found [?]. The other spatial dimension can be treated in the same way and the results are the same. Confinement in the axial direction z is purposely weaker, and ions will align in this direction. Two electrodes with constant potential U are present, they create a harmonic potential

$$V = \frac{1}{2}m\omega_z^2 z^2, \quad (2.3.7)$$

where ω_z is the axial trap frequency. In the case of a string of ions, mutual repulsions must also be included, in the next section we will consider this case.

2.3.2 Ion strings

For the goals of this thesis, we are interested in the separation between N ions loaded in the trap. This will give us an idea of how narrowly the beam should be focused and will set an appropriate problem spatial scale.

Let us consider the z direction where the ions are more weakly confined such that they form a string. The potential can be approximated as harmonic and hence given by

$$V = \sum_{i=0}^N \frac{1}{2}m\omega_z^2 z_i^2 + \sum_{i \neq j}^N \frac{Z^2 e^2}{8\pi\epsilon_0} \frac{1}{|z_i - z_j|}, \quad (2.3.8)$$

where z_i is the position of the i -th ion, and Z the degree of ionization of the ions. The equilibrium positions can be found at the minima of the potential, i.e. where the first derivative zeros

$$\frac{\partial V}{\partial z_i} = 0 \implies u_i - \sum_{j=1}^{i-1} \frac{1}{(u_i - u_j)^2} + \sum_{j=i+1}^N \frac{1}{(u_i - u_j)^2} = 0, \quad (2.3.9)$$

where we defined the dimensionless quantity $u_i = z_i/l$ and $l^3 = \frac{Z^2 e^2}{4\pi\epsilon_0 m \omega^2}$. The last equation can be solved analytically for 2 or 3 ions [?]. For the case $N = 2$ we get the system

$$\begin{cases} u_1 + \frac{1}{(u_1 - u_2)^2} = 0 \\ u_2 + \frac{1}{(u_1 - u_2)^2} = 0 \end{cases} \implies u_1 = -u_2, \quad u_1 = \left(\frac{1}{2}\right)^{2/3} \simeq 0.629 \quad (2.3.10)$$

For ${}^{40}\text{Ca}^+$ ions (atomic mass 39.96259098(22) u [?]) in a Paul trap with axial confinement of $\omega_z = 2\pi \times 1$ MHz, we have $l \simeq 4.45 \times 10^{-6}$ m, which means that 2 ions are separated by $\simeq 5.6 \mu\text{m}$. This size is accessible since it is above diffraction limit for optical atomic transitions. In figure 2.3.2 ions positions are presented for different number of ions N trapped with an axial confinement of $\omega_z = 2\pi \times 1$ MHz.

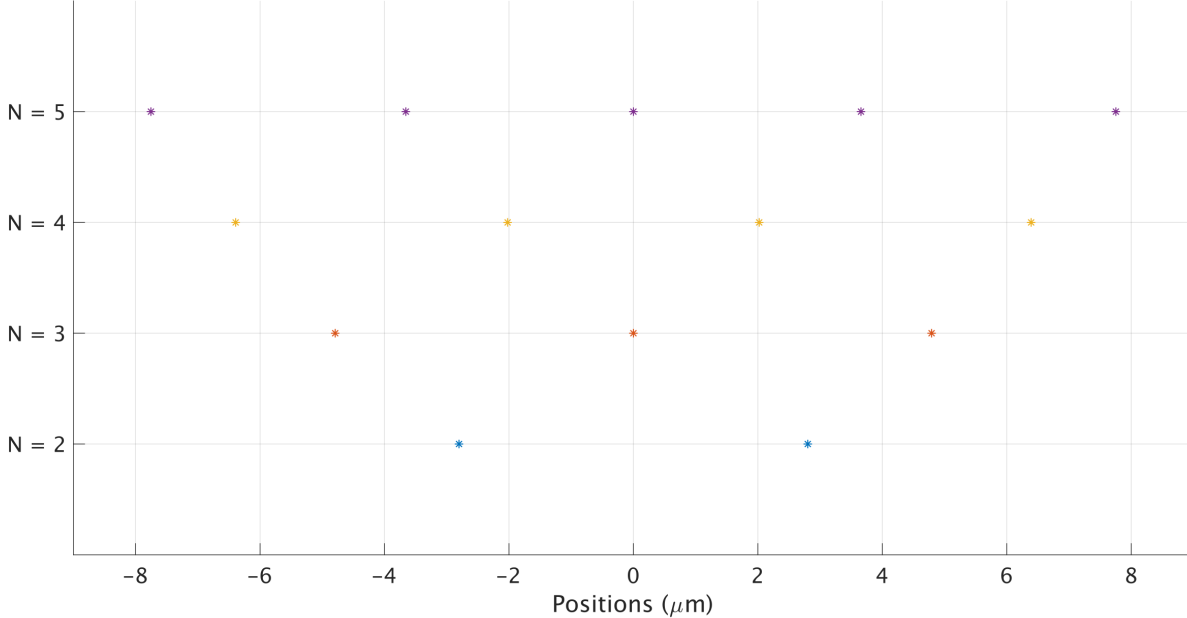


Figure 2.3.2: Ions position for different number N of ions in the trap. Confinement is $\omega_z = 2\pi \times 1$ MHz.

2.3.3 Doppler cooling

Coherent manipulation of ions requires cooling them to reach at least the Lamb Dicke regime [?], where the extend of the ion wave packet is much smaller than the optical wavelengths of the lasers. Several techniques are available for cooling, but the most popular

and more frequently used is Doppler cooling. The idea comes from neutral atoms [?] and can be applied to ions as well: a laser interacts with a particular transition, exchanging a photon and therefore giving a momentum kick $\Delta p = \hbar\mathbf{k}$ in a particular direction to the ion. The absorbed photon is given back through spontaneous emission in a random direction, giving another kick to the ion. Over many cycles of absorption and emission, the random kick due to emission will average to zero, while the kick given by the laser will accumulate slowing down and cooling the ion in the direction of the laser.

The master equation (2.1.25) can be explicitly written for every component of the density matrix ρ , in the rotating frame they are called optical Bloch equations and they are

$$\frac{d\rho_{ee}}{dt} = -i\frac{\Omega}{2}(\rho_{eg} - \rho_{ge}) - \Gamma\rho_{ee} \quad (2.3.11)$$

$$\frac{d\rho_{gg}}{dt} = i\frac{\Omega}{2}(\rho_{eg} - \rho_{ge}) + \Gamma\rho_{ee} \quad (2.3.12)$$

$$\frac{d\rho_{ge}}{dt} = -\left(\frac{\Gamma}{2} + i\Delta\right)\rho_{ge} - i\frac{\Omega}{2}(\rho_{ee} - \rho_{gg}) \quad (2.3.13)$$

$$\frac{d\rho_{eg}}{dt} = -\left(\frac{\Gamma}{2} - i\Delta\right)\rho_{eg} + i\frac{\Omega}{2}(\rho_{ee} - \rho_{gg}) \quad (2.3.14)$$

We are interested in the steady state case, i.e. when the system reaches the equilibrium. Therefore, we look at $\rho_{ee}(t \rightarrow \infty)$, the solution of equation (2.3.11) is

$$\rho_{ee}(t \rightarrow \infty) = \frac{\Omega^2/\Gamma^2}{1 + \left(2\frac{\Delta - \mathbf{k} \cdot \mathbf{v}}{\Gamma}\right)^2 + 2\frac{\Omega^2}{\Gamma^2}} \quad (2.3.15)$$

where Δ is the detuning, and v the velocity of the ions. The force exerted on the ions, due to the radiative pressure, is proportional to this population as

$$F = \hbar k \Gamma \rho_{ee} \simeq F_0 + \frac{dF}{dv}v = \hbar k \Gamma \frac{\Omega^2}{\Gamma^2 + 4\Delta^2} + F_0 \frac{8k\Delta}{\Gamma^2 + 4\Delta^2}v \quad (2.3.16)$$

where we assumed low velocities $v \simeq 0$ and thus linearized the equation. The effect of the constant term in the force is just to displace the ion from its central position. Instead, the linear term acts as a viscous friction that cools the ions with a rate of $\dot{E}_c = \langle Fv \rangle$. If on one side spontaneous emission allows for Doppler cooling, it also sets the lower limit. The small fluctuations in the Brownian motion leads to diffusion which heats the ion at a rate of

$$\dot{E}_h = \frac{1}{m} \frac{d}{dt} \langle p^2 \rangle = \frac{1}{m} (\hbar k)^2 \Gamma \langle \rho_{ee}(v) \rangle. \quad (2.3.17)$$

At equilibrium, the heating rate equals the cooling rate giving the lowest temperature achievable

$$\dot{E}_h + \dot{E}_c = 0 \implies k_B T = -\frac{\hbar\Gamma}{4} \left(\frac{\Gamma}{2\Delta} + \frac{2\Delta}{\Gamma} \right). \quad (2.3.18)$$

From here it is clear that by choosing the appropriated detuning, it is possible to reach the lowest temperature

$$T_{min} = \frac{\hbar\Gamma}{2k_B}, \quad \text{for } \Delta = -\frac{\Gamma}{2}. \quad (2.3.19)$$

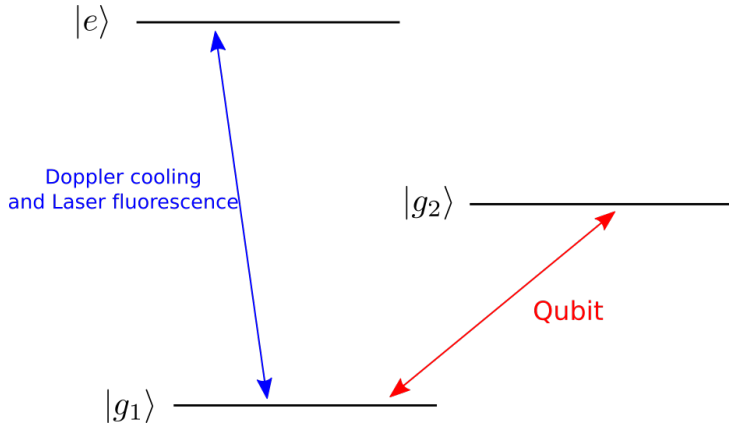


Figure 2.3.3: Λ type scheme. Two ground states $|g_1\rangle$ and $|g_2\rangle$ are stable or metastable, while the excited level $|e\rangle$ is short lived. Qubit is encoded in the two ground states while laser fluorescence and laser cooling is done on the $|g_1\rangle \rightarrow |e\rangle$ transition. The transition $|e\rangle \rightarrow |g_2\rangle$ is repumped to avoid for the electron to be stuck in g_2 .

At this temperature, the average phonon number is $\langle \hat{n} \rangle = \Gamma / 2\omega_z$ [?]. As an example, calcium ions confined in a trap with $\omega_z = 2\pi \times 1$ MHz, can be cooled using the transition $|\text{S}_{1/2}\rangle \rightarrow |\text{P}_{1/2}\rangle$ ($\Gamma = 2\pi \times 20.8$ MHz), the Doppler temperature is $T_{min} \sim 500 \mu\text{K}$, and the corresponding average phonon number is $\langle \hat{n} \rangle = 10.4$. The wavefunction extend for this phonon number can be found as the standard deviation of the operator \hat{z} for the vibrational state $|n\rangle$, creation and annihilation operator algebra gives

$$\sigma_z = \sqrt{\langle \hat{z}^2 \rangle} = \sqrt{\frac{\hbar}{2m\omega_z}(1 + 2\langle \hat{n} \rangle)} \simeq 52.5 \text{ nm.} \quad (2.3.20)$$

An ion cooled with Doppler cooling therefore has a spatial dimension still much smaller than the ion separations.

To further decrease $\langle \hat{n} \rangle$, sideband cooling is used [?], here particular sideband transitions are excited to reduce the phonon number of the ions inside the trap. However in the experiments of this thesis, only Doppler cooling has been performed.

2.4 Laser beam

2.4.1 Gaussian beams

Lasers emit light in the shape of Gaussian beams, so it is import to understand what Gaussian beams are and their characteristics. In this chapter we will take a closer look into such beams and introduce important quantities to characterize a Gaussian beam. From a theoretical point of view, Gaussian beams are a particular solution of the Helmholtz equation $(\nabla^2 + k^2)U(\mathbf{r}) = 0$, with k being the wavevector, and $U(\mathbf{r})$ the complex electric field. If we can consider a wave propagating in the z direction, we can write it as [?]:

$$U(\mathbf{r}) = A_0 \frac{W_0}{W(z)} \exp \left\{ -\frac{x^2 + y^2}{W^2(z)} \right\} \exp \left\{ -ikz - ik \frac{x^2 + y^2}{2R(z)} + i \arctan(z/z_0) \right\}. \quad (2.4.1)$$

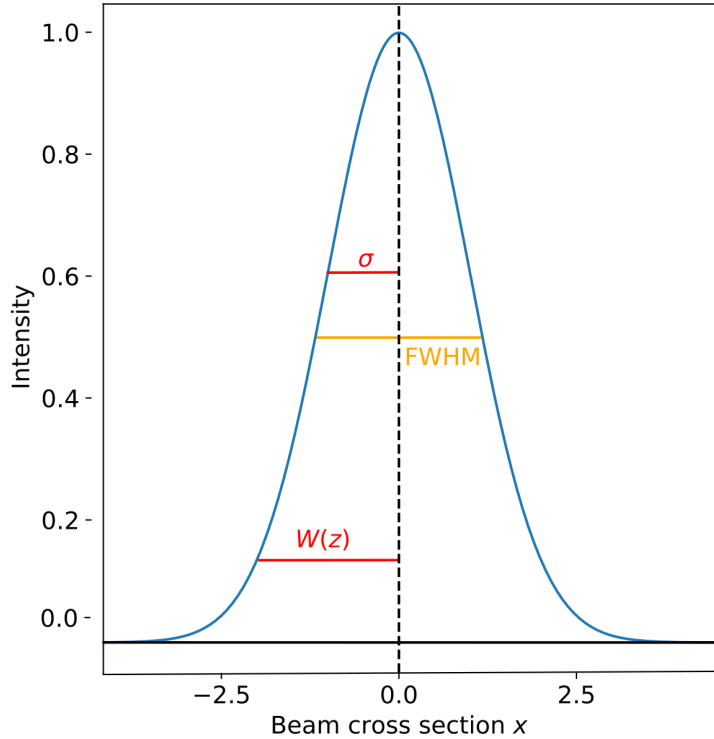


Figure 2.4.1: Intensity of a Gaussian beam, x cross section. The beam is normalized and $\sigma = 1$. Graphical representations of used widths are displayed: $W(z)$ is defined as the point at which the intensity I has fallen to $1/e^2 = 13.5\%$ of its maximum value; σ is the standard deviation of a Gaussian in the form $Ae^{-\frac{x^2}{2\sigma^2}}$; FWHM is the full width half maximum. Relationships among these quantities are: $W(z) = 2\sigma$, and $W = 0.84 \cdot \text{FWHM}$.

This is the form of Gaussian beams, they are characterized by an amplitude A_0 , a width $W(z)$, Rayleigh range z_0 , and a curvature radius $R(z)$. Let us take a look at the features that arise from this shape. The intensity can be calculated by taking the square of the complex amplitude

$$I(\mathbf{r}) = |U(\mathbf{r})|^2 = I_0 \left(\frac{W_0}{W(z)} \right)^2 \exp \left\{ \frac{2x^2 + 2y^2}{W^2(z)} \right\} \quad I_0 = |A_0|^2. \quad (2.4.2)$$

It is clear from here why the beam is called Gaussian. For a fixed z , i.e. the sections in the $x - y$ plane are shaped as a two dimensional Gaussian distribution. Therefore, one dimensional Gaussian can be found as cross section of the 2D profile. For simplicity, let us take the profile for a fixed z and $y = 0$, this takes the form

$$I(x, y = 0, z) = \tilde{A}(z) \exp \left\{ \frac{2x^2}{W^2(z)} \right\} \quad \tilde{A}(z) = I_0 \left(\frac{W_0}{W(z)} \right)^2. \quad (2.4.3)$$

In figure 2.4.1, the x cross section is depicted for this intensity profile normalized in amplitude. Parameters used to measure the width are also displayed and defined in the caption. All of those quantities are equivalent and differ only by a prefactor, so for the rest of the section, we stick to $W(z)$ and study its behaviour. From Helmholtz equation

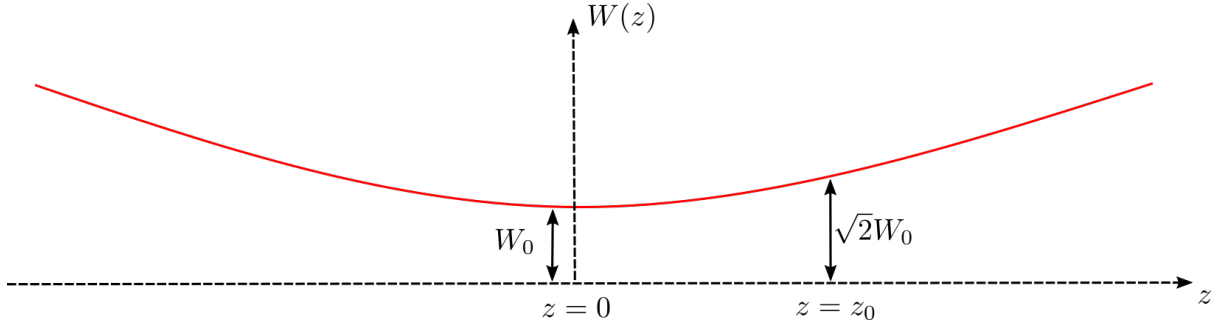


Figure 2.4.2: Width profile of a Gaussian beam, equation (2.4.4). The beam is focused at the position $z = 0$, here it assumes the minimum width W_0 , also referred to as waist. z_0 is the Rayleigh range where the width is $\sqrt{2}W_0$

[?], the profile of $W(z)$ as a function of z is found to be

$$W(z) = W_0 \sqrt{1 + \left(\frac{z}{z_0}\right)^2} \quad W_0 = \sqrt{\frac{\lambda z_0}{\pi}} \quad z_0 = \frac{\pi W_0^2}{\lambda}. \quad (2.4.4)$$

λ is the wavelength, and W_0 and z_0 are respectively the waist of the beam and the Rayleigh range discussed below.

There are important features to be noticed with reference to figure (2.4.2): The width $W(z)$ assumes its minimum value W_0 at $z = 0$, this spot is called focus and its width W_0 is the waist of the beam. The Rayleigh range z_0 gives an idea of how quickly the beam is expanding. Mathematically z_0 is the distance between the focus and the point where the width $W(z)$ is exactly $\sqrt{2}W_0$. For $z \gg z_0$, the beam profile diverges almost linearly with an angle given by $\theta = W_0/z_0$, which means the smaller the focus, the greater it diverges. This property will become important later in the work, because it provides one limit on the focus spot. In fact, the optical aperture of the trap is limited by the electrodes, and a beam that diverges too rapidly can potentially clip on one electrode causing aberrations and scattered light in the trap.

A Gaussian beam can be shaped using optical elements. In order to study such reshaping, let us consider a thin spherical lens with focal length f , and radius of curvature R_l placed at position z . The effect of the lens on the beam is to give an extra phase factor $k(x^2 + y^2)/2f$ to equation (2.4.1) [?]. We can match the phase of the incoming and emerging waves, which have respectively radius of curvature R , and R' , this results in

$$\frac{1}{R'} = \frac{1}{R} - \frac{1}{f}. \quad (2.4.5)$$

The effect of the lens is to change the radius of curvature to R' . Moreover, the width of the beam at the lens is not altered $W = W'$. Using these last two facts, we can determine all the parameters of the outgoing wave. The most important for us is the new waist W'_0

$$W'_0 = M W_0 \quad M = \frac{M_r}{\sqrt{q + r^2}} \quad M_r = \left| \frac{f}{z - f} \right| \quad r = \frac{z_0}{z - f}. \quad (2.4.6)$$

M is the magnification factor which provides an easy way to describe the change of the beam. For a better understanding of this last result, let us consider an less general example. We place the lens at the focus $z = 0$, and have a collimated beam $z_0 \rightarrow +\infty$. In

this case the new waist is

$$W'_0 = \frac{W_0}{\sqrt{1 + (z_0/f)^2}} \simeq W_0 \frac{f}{z_0} = \frac{\lambda f}{\pi W_0} \quad (2.4.7)$$

where the approximation comes from taking $z_0 \gg f$. There are three parameters we can act on to achieve the smallest focus spot: (a) the wavelength λ , the shorter the better; (b) the focal length of the lens f , smaller focus with shorter focal length; (c) the waist of the incoming beam W_0 , larger waist corresponds to narrower focus.

An optical system performing to the theoretical limit is said to be diffraction limited. In the instance of a focusing system, it corresponds to the case where the collimated beam diameter $2W_0$ is equal to the diameter D of the focusing lens. Equation 2.4.7 becomes

$$W_0 = \frac{2\lambda}{\pi} \frac{f}{D}. \quad (2.4.8)$$

If the size of the collimated beam is further increased, the lens becomes a finite size aperture and diffraction effects will appear at the image plane.

2.4.2 Beam steering via Acousto-optical Deflectors

An acousto-optical deflector (AOD) is a common device that can change the propagation direction of a laser beam, typically on the few microsecond timescale. In this work we use an AOD to change which ion is illuminated by a single-ion focused laser. The working principle of an AOD is based on the Acousto-optical effect. A piezo is used to create acoustic waves that propagate through a crystal. The waves modify the crystal refractive index, creating a periodic optical grating that can deflect light travelling through it. Following the approach of [?] to model the device, let us consider a rectangular crystal like in figure 2.4.3. The acoustic wave creates a sinusoidal pattern with frequency Ω_s and wavevector q , for the refractive index $n(x, t)$

$$n(x, t) = n - \Delta n_0 \cos(\Omega_s t - qx), \quad (2.4.9)$$

where n is the refractive index of the unperturbed medium, Δn_0 is the amplitude of the perturbation. Δn_0 is proportional to the square root of the sound intensity. The complex amplitude of the refracted wave r can be calculated by dividing the crystal in thin layers, each with his refractive index $n(x)$. The total refraction is given by all the contributions $\frac{dr}{dx}$ of every layer, we can therefore integrate in the x direction over the length L as follow:

$$r = \int_{L/2}^{L/2} e^{i2kx \sin \theta} \frac{dr}{dx} dx \quad (2.4.10)$$

The included phase takes into consideration the different phase of the input beam when different layers are met. The integral can be solved with a change of variable

$$\frac{dr}{dx} = \frac{dr}{dn} \frac{dn}{dx} = \frac{dr}{dn} q \Delta n_0 \sin(\Omega_s t - qx), \quad (2.4.11)$$

The sine function can be written as exponential and now the integral contains only exponential functions which are trivial to calculate. At the end we obtain two contributions

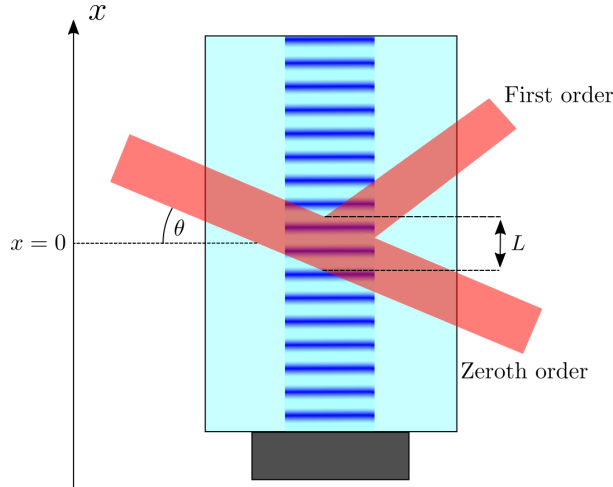


Figure 2.4.3: Simple model of an AOD. In black at the bottom a black piezo that generates acoustic waves through the light blue crystal. In red, a collimated beam of light enters in the crystal with an angle θ and gets partially deflected due to the interaction with the effective optical grating created by the acoustic waves.

for the refracted wave r :

$$r = r_+ + r_- \quad r_{\pm} = \pm ir_0 \text{sinc} \left[(2k \sin \theta \mp q) \frac{L}{2\pi} \right] e^{\pm i\Omega_s t} \quad (2.4.12)$$

These two terms are the plus and minus first order diffraction, an acousto-optical device can be operated symmetrically entering either with a positive angle or with a negative one. Since the maths and the physics is the same, we will focus only on the positive term, called upshifted Bragg diffraction. The sinc function peaks sharply when its argument is 0, i.e. at $2k \sin \theta = q$, and then quickly decreases as the angle is changed. Hence, the input beam must enter with a particular angle in order to diffract with maximum efficiency. The condition to be satisfied is called Bragg condition, and can be written as a function of the optical λ and acoustic Λ_s wavelengths as

$$\sin \theta = \frac{\lambda}{2\Lambda_s} \quad \Lambda_s = \frac{2\pi}{q}. \quad (2.4.13)$$

If the condition is not perfectly matched, some light will not be diffracted and will be transmitted unaltered through the device. The ratio of the transmitted and diffracted light is called diffraction efficiency and gives an idea of how well an acousto-optical device is performing.

From equation (2.4.12) we can notice that an extra phase factor proportional to $\Omega_s t$ is added to the reflected wave. Thus, if the incoming wave is oscillating at $\propto e^{i\omega t}$, the diffracted wave will oscillate as $\propto r_+ e^{i\omega t} \implies \propto e^{i(\omega + \Omega_s)t}$. The frequency of the diffracted wave ω_r is therefore shifted by the frequency of the acoustic vibration as

$$\omega_r = \omega + \Omega_s. \quad (2.4.14)$$

The acousto-optical effect described above is common to different devices optimized for specific tasks. Two of the most commons devices are Acousto-optical Deflectors (AOD) and Acousto-optical Modulators (AOM). The idea of the latter is to shift the frequency

of a laser using equation (2.4.14). Deflectors instead exploit the fact that the deflection angle θ changes linearly as a function of the acoustic frequency Ω_s . Assuming that the angle θ is small enough to approximate $\sin \theta \sim \theta$, the Bragg condition can be written as

$$\theta \simeq \frac{\lambda}{2v_s} f, \quad (2.4.15)$$

where v_s is the speed of sound and f the frequency of the acoustic wave. We can already see that if we change the frequency f , the deflection angle θ changes proportionally. Although the Bragg condition (2.4.13) is not satisfied anymore, we can work with small enough angles that the diffraction efficiency remains above a certain threshold. The bandwidth B specifies the range of frequencies over which deflectors work.

AOMs and AODs differ by the relative divergence of the optical and acoustic beam [?], moreover for AODs, speed and the number of resolvable spots are more important, while for AOM's the optimization is on modulation bandwidth. These different priorities in building the devices influence the choice of the crystal and acoustic mode, for instance, a slow acoustic velocity and shear mode are preferred in AODs [?]. More advanced techniques to engineer an AOD are available, for example the piezo is replaced by a phase array of transducers that tilt the acoustic beam [?].

As already stated, in the experiment setup of this work, an AOD is used to steer a single-ion focused laser and aim at different ions in the μs timescale. AOMs instead are extensively used to tune and scan the laser frequencies.

2.5 Experiments model

The aim of this thesis is to perform two experiments with ions: qubit manipulation, and photon generation. In addition to test these two functionalities, the experiments are also designed to asses the performance of the addressing system as discussed below. In both cases a string of 3-4 ions is loaded in the trap, the addressed Raman laser is focused on a single ion and experiments are carried out.

2.5.1 Addressed qubit manipulation

As we have seen, ions can be used to encode and process quantum information. As highlighted in figure 5.3.1, the qubit is encoded in the $|S\rangle \rightarrow |D\rangle$ transition. The 393nm transition from $|S\rangle \rightarrow |P\rangle$ can be used to induce a phase shift on the ground state of the qubit $|S\rangle$. In the off resonant regime, the laser induces a Stark shift $\delta = \Omega^2/4\Delta$ without actually exciting the state. As discussed in section 2.1.2.2, in order for this to happen, we should have $\delta \gg \Gamma_{eff}$. Therefore in the experiment we decided to set the detuning such that the ratio between the Stark shift and the spontaneous scattering rate is 100

$$\frac{\delta}{\Gamma_{eff}} = \frac{2\Delta}{\Gamma} \sim 100 \implies \Delta \sim 3 \text{ GHz}. \quad (2.5.1)$$

Furthermore, ions can be used as sensitive tools for beam profiling, the addressed manipulation changes only the qubit state of a single ion. Hence, by measuring the state of all ions, and scanning the beam across the ions string, a beam profile can be obtained. In a single experiment we can therefore characterize the beam and demonstrate

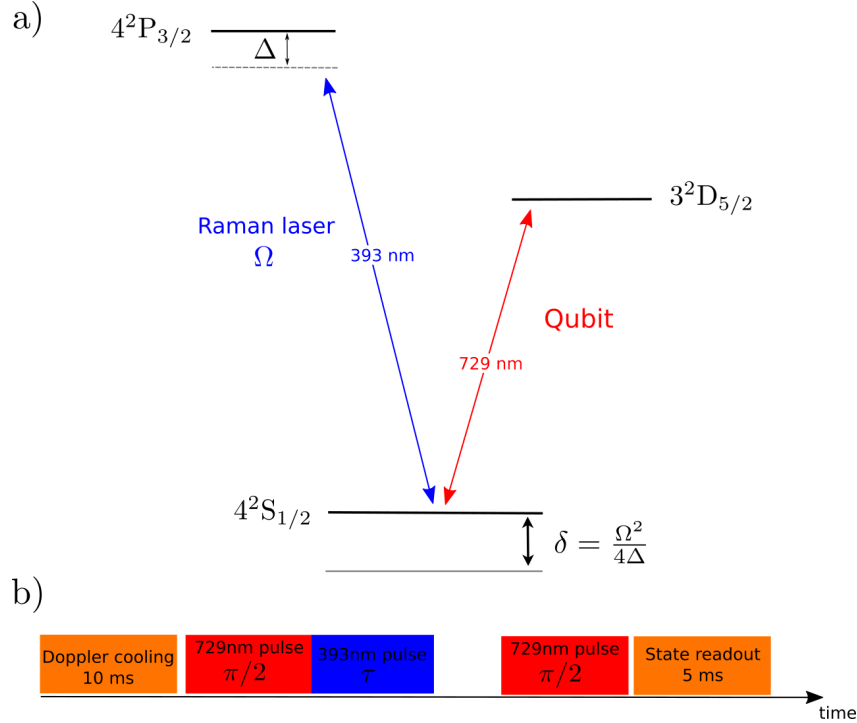


Figure 2.5.1: a) Relevant levels for the experiment, the qubit is encoded in the 729 nm transition, the 393 nm laser is used to shift the $|S\rangle$ level via AC Stark shift b) Experiment pulse sequence, Doppler cooling and state readout are described in section 3.1.2. The time τ had a variable length.

qubit manipulation. The experiment consists of Ramsey interferometry, already performed in the past to measure AC Stark shift [16]. In summary, the idea is to send a resonant $\pi/2$ pulse at 729 nm, which brings the qubit state to a superposition $|S\rangle + |D\rangle$, here another in phase resonant $\pi/2$ pulse at 729 nm would bring the final state to the excited level $|D\rangle$. However, if between the two 729 nm pulses, AC stark shift is induced by a pulse of 393 nm light, an additional phase is added to the superposition $|S\rangle + |D\rangle$, and the final state after the second 729 nm pulse will depend on the shift induced by the 393nm laser. The phase of the second 729 nm pulse can also be varied. By calculating the final probability P_D it is possible to infer the Rabi frequency of the 393 nm light. Rigorous mathematic can be done with matrices (2.1.15) here called U_{729} and (2.1.20), referred to as U_{393} . After the three pulse sequence the final state is

$$\begin{aligned} |\psi_f\rangle &= U_{729}(\pi, \phi)U_{393}(\delta)U_{729}(\pi, 0)|S\rangle \\ &= \frac{1}{2} \left(e^{-i\frac{\delta}{2}\tau} - e^{-i\phi} \right) |S\rangle - \frac{i}{2} \left(1 + e^{-i\frac{\delta}{2}\tau} e^{-i\phi} \right) |D\rangle \end{aligned} \quad (2.5.2)$$

where $\delta = \Omega^2/4\Delta$ is the Stark shift, and Ω is the Rabi frequency of the 393nm light that we want to measure. The final probability is then

$$P_D = \cos^2 \left(2\phi + 2\frac{\delta\tau}{2} \right) = \cos^2 \left(2\phi + \frac{\Omega^2\tau}{4\Delta} \right). \quad (2.5.3)$$

As we can see, the final signal depends on the phase of the second 729nm pulse ϕ and on the Stark shift induced by the 393nm laser. To get Ω^2 a simple formula inversion can be

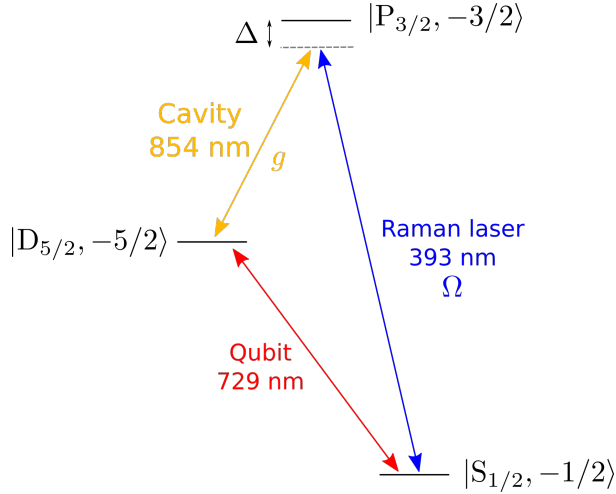


Figure 2.5.2: Scheme of the Raman process used to generate photons, via a cavity enhanced Raman process (Section 2.2.3). The electron in the $|S\rangle$ state is excited to the $|D\rangle$ level by absorbing a 393 nm photon and emitting a 854 nm photon in the cavity.

done

$$\Omega^2 = \left[\arccos \left(\sqrt{P_D} \right) - 2\phi \right]. \quad (2.5.4)$$

The phase ϕ can be set experimentally and all constants have been dropped as the data will be normalized. The experiment sequence is in figure 5.3.1. For every sequence, a stage of Doppler Cooling at the beginning is included and at the end of the pulses state readout with single-ion resolving camera is performed. For each 393 nm pulse length τ the sequence is repeated $N = 50$ times to obtain and estimate the electronic excitation probability.

2.5.2 Addressed photon generation

The second experiment consists of generating photons from one single ion, using the Raman process described in section 2.2.3. In figure 2.5.2 the relevant levels are depicted. In this case the ion is positioned in a maximum of the cavity electric field such that the coupling atom-cavity g is maximized. A 393 nm laser pulse triggers the generation of a photon in the cavity through a Raman process as described in section 2.2.3. The detunings of the cavity and laser pulse must be equal, moreover the detuning should be large enough to adiabatically eliminate the P state and avoid spontaneous scattering. As seen in section 2.2.3, this is ensured by a detuning of $\Delta \sim 400$ MHz. In this process the population of the state $|S\rangle$ is coherently transferred to the $|D\rangle$ state by absorbing a 393 nm photon and emitting a 854 nm photon in the cavity, the photon then exits from the cavity. The states involved in the dynamics are

$$|S_{1/2}, -1/2\rangle \rightarrow |P_{3/2}, -3/2\rangle \rightarrow |D_{5/2}, -5/2\rangle. \quad (2.5.5)$$

Note that the effective Rabi frequency of the population transfer is proportional to the laser drive Rabi frequency $\propto \Omega$ as seen in equation (2.2.7). On the contrary, AC Stark shift depends on the Intensity $\propto \Omega^2$. Therefore, the addressing error in the two experiments are different. After the excitation and photo emission, state detection on all ions is performed, this gives the possibility to check if other ions have been unwantedly addressed.

Chapter 3

Existing experimental system

In this chapter we are going to describe the essential parts of the already existing setup on top of which the addressing system has been built. Calcium-40 ions are used in the experiment, the implementation of several techniques for trapping and manipulating these ions are discussed. Furthermore, the addressing setup utilizes 393 nm light, the laser emitting this light was already installed by H. Hainzer¹ [?], thus that setup is briefly presented. The experiment can be controlled remotely via computers, an overview of how it is implemented and how it works is also given.

3.1 Ion trap and key techniques

3.1.1 Calcium Ions

For quantum computation purposes, ions with a single valence electron are an attractive choice, examples include beryllium [?], barium [?], strontium [?], calcium [?]. Other trapped species include for example ytterbium [?], and magnesium [?]. In our experiment we trap $^{40}\text{Ca}^+$, the most abundant isotope of calcium. In figure 3.1.1 the level scheme of the valence electron is presented. We use the notation $n^{2s+1}l_j$, where n is the principal quantum number, s the electron spin, l the orbital angular moment, and $j = |l \pm s|$ the total angular moment. In the experiment a magnetic field lifts the level degeneracy, thus the magnetic m_j quantum number is also present. A ground state $S_{1/2}$ is present with no hyperfine structure as $^{40}\text{Ca}^+$ does not posses a nuclear spin. Two short lived excited states ($1/\Gamma \sim 7$ ns) $P_{1/2}$, and $P_{3/2}$ are connected to S via dipole transitions. Due to the short lifetimes of these two states, they are suitable for laser cooling and state detection. The states $D_{3/2}$ and $D_{5/2}$ are metastable ($1/\Gamma \sim 1$ s) and are coupled to the S state via electric quadrupole transitions. An optical qubit can be implemented in the transition $S_{1/2} \rightarrow D_{5/2}$, as the lifetime of the $D_{5/2}$ state is longer than typical operation times [?]. Other choices for qubit implementation have been explored, for instance in the Zeeman levels of the $S_{1/2}$ manifold [?]. Table 3.1.1 summarizes details about the different transitions, and what they are used for. A more detailed description and implementation is discussed in the next section.

¹In her work, the 393 nm laser (MSquared Ti:Sa) and the ion cavity were locked to an ultrastable reference cavity. She measured the linewidth of the MSquared Ti:Sa laser to be <100 Hz with a drift rate of 202(1) mHz/s

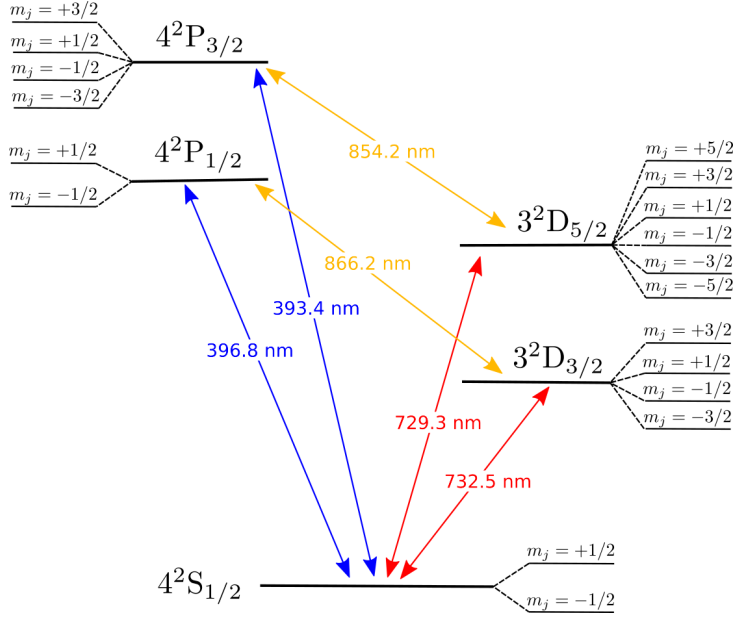


Figure 3.1.1: Level scheme of $^{40}\text{Ca}^+$ with main transitions highlighted and Zeeman substructure. Blue transitions are dipole transitions suitable for cooling, and imaging. Red transitions are dipole forbidden, but accessible via electric quadrupole, they are used to encode qubits. Orange transition are usually repumped. In addition, the 854 nm transition is tuned in resonance with the cavity for photon generation purposes. From more and precise value see table 3.1.1

Transition	λ (nm)	Decay rate Γ	Lifetime τ	BR	Main use
$S_{1/2} \leftrightarrow P_{1/2}$	396.847	$2\pi \times 20.8$ MHz	7.7 ns	94%	Cooling and imaging
$S_{1/2} \leftrightarrow P_{3/2}$	393.366	$2\pi \times 21.4$ MHz	7.4 ns	94%	Photon generation
$S_{1/2} \leftrightarrow D_{3/2}$	732.389	$2\pi \times 0.132$ Hz	1.080 s	-	-
$S_{1/2} \leftrightarrow D_{5/2}$	729.147	$2\pi \times 0.136$ Hz	1.045 s	-	Qubit
$P_{1/2} \leftrightarrow D_{3/2}$	866.214	$2\pi \times 1.70$ MHz	94.3 ns	6%	Repumping
$P_{3/2} \leftrightarrow D_{5/2}$	854.209	$2\pi \times 1.34$ MHz	101 ns	5.3%	Cavity photon
$P_{3/2} \leftrightarrow D_{3/2}$	849.802	$2\pi \times 1.52$ MHz	902 ns	0.6%	Repumping

Table 3.1.1: Transitions in $^{40}\text{Ca}^+$ and current use in the experiment. λ is the wavelength of the transition, and BR is the branch ratios for the different decay channels. Values are taken from [?, ?]

3.1.2 Trapping, cooling, and state readout

In this section we discuss how to implement important techniques for ion based quantum computing and we collect parameters of our experiment.

TRAPPING AND LOADING

Our trap is a linear 3D RF Paul trap as depicted in figure 2.3.1, the picture of the real trap is displayed in figure 3.1.2 where main components are highlighted. The electrodes are made in titanium, and are covered in gold. The trap itself is mounted vertically on a Shappire holder. The endcaps are 5 mm apart, and they are usually kept at voltages on the



Figure 3.1.2: Photo of the mounted trap. Axial direction is defined along the z axis, while radial is $r^2 = x^2 + y^2$. Highlighted in the image there are: (A) Trap's golden blades for radial RF confinement (B) One pair of compensation electrodes (C) Cavity mirrors, right mirror is highly reflective, left is 854 nm photon output mirror (see section 2.2.2), separation is ~ 20 mm (D) Calcium atomic oven (E) Collimation lenses (F) Static voltage endcaps for axial confinement.

order of 500-1000V, which corresponds to single-ion axial frequencies of $\omega_z \sim 2\pi \times 0.7 - 1$ MHz respectively. The four blades are 0.8 mm from the center of the trap and driven with an RF of ~ 24 MHz. The RF signal from an amplifier is impedance matched with the trap using a quarter-wave bulk helical resonator (not shown). The trap also includes three pairs of compensations electrodes that can be used to compensate for stray electric fields, top view of the trap with compensations electrodes is in figure 4.3.4.

Loading of ions is done with an atomic oven, calcium is heated and directed towards the trap, where neutral atoms undergo 2-stage photon ionization. One laser 422 nm, resonantly excites one electron to the state $4p^1P_1$, while a second laser 375 nm, brings the electron to free space ionizing the atoms [?]. Such two stage process allows to filter for isotopes ionizing only ^{40}Ca . Loading usually takes minutes or tens of minutes depending on the number of ions one wants to load. Storing time can be in the order of days, especially when a single ion is loaded.

COOLING

Once loaded, ions are Doppler laser cooled with 397 nm light on the transition $S_{1/2} \rightarrow P_{1/2}$ detuned between $-\Gamma/2$ and resonance². An additional repumper on the transition $P_{1/2} \rightarrow D_{3/2}$ is also used to avoid the electron being stuck in the $D_{3/2}$ state. For typical experiments a stage of Doppler cooling is always included, this lasts from 1 millisecond up to tens of milliseconds.

IMAGING

With the same Doppler cooling light, imaging can also be done. The light shines on

²The choice of cooling closer to resonance is to collect more photons on the camera

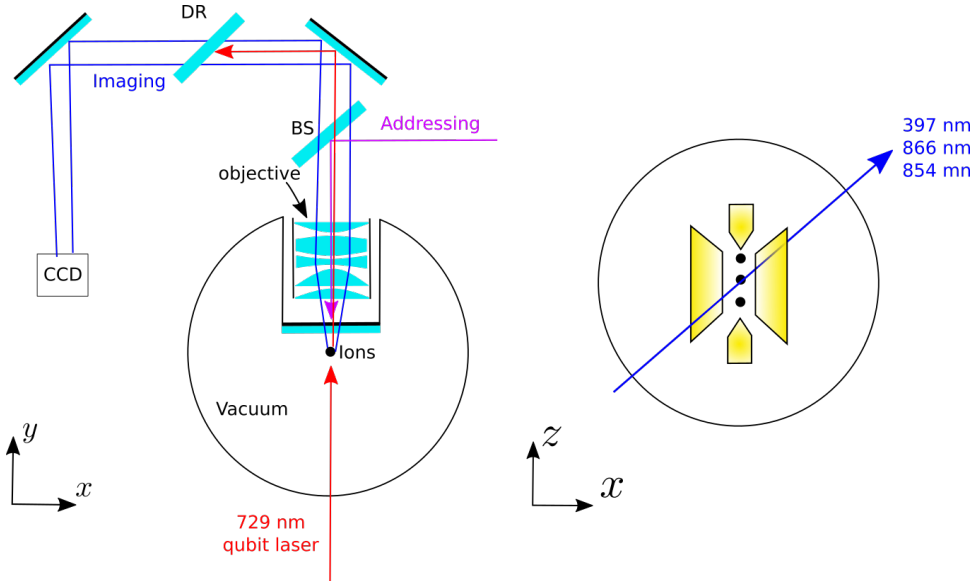


Figure 3.1.3: Left: top view of the experiment, an out of vacuum objective collimates and focuses the scattered photons onto the CCD camera, ~ 1.5 m away from the ions. The addressing setup must share part of this path, as the same objective is used for focusing. A beam splitter (BS), installed during the course of this thesis, separates the imaging path from the addressing path. More details about the addressing path are in section 4.1. A dichroic mirror (DM) reflects the 729 nm light such that only 393 nm light can reach the camera. Right: front view of the trap, other lasers direction are depicted.

the ions exciting the transition $S_{1/2} \rightarrow P_{1/2}$ driving the electron to the excited state which then decays spontaneously emitting photons. Photons are collected with a custom objective with NA of ~ 0.289 , which means an efficiency of 2.5 % over the solid angle 4π . The objective focuses the collected photons 1.5 meters away where a CCD camera (Andor iXon Ultra 897) is placed. The geometrical path of the imaging is displayed in figure 3.1.3, this setup has a magnification factor of ~ 18.6 . The same objective is also used for the addressing setup built within this thesis. Therefore, the imaging optical path must be partially shared with the newly built addressing. More details of the objective are given in section 4.2.

STATE READOUT WITH CAMERA

Consider a qubit encoded in the states $S_{1/2} \rightarrow D_{5/2}$, if the imaging laser is switched on, the electron will be projected either to the $S_{1/2}$ level or to the $D_{5/2}$. In the first case, photons are scattered from the ion and collected on the camera, in the second case the electron is shelved and will not scatter any photon. Hence, the two cases are distinguishable by the brightness on the camera. The camera can spatially separate the ions and therefore distinguish the individual state of each ion in the string. In order to perform this task, the camera software³ needs initial calibration, this means that a region of interest, where the fluorescing ions are, is first selected. The camera then integrates in one direction and tries to fit a number of Gaussian equals to the number of ions, the central value of each peak indicates the position of each ions. During the camera read out the software measures the brightness at these spots and compares it with a previously set threshold determining ultimately the ion state.

³Home developed software that works together with TrICS, see section 3.3

3.2 393 nm laser

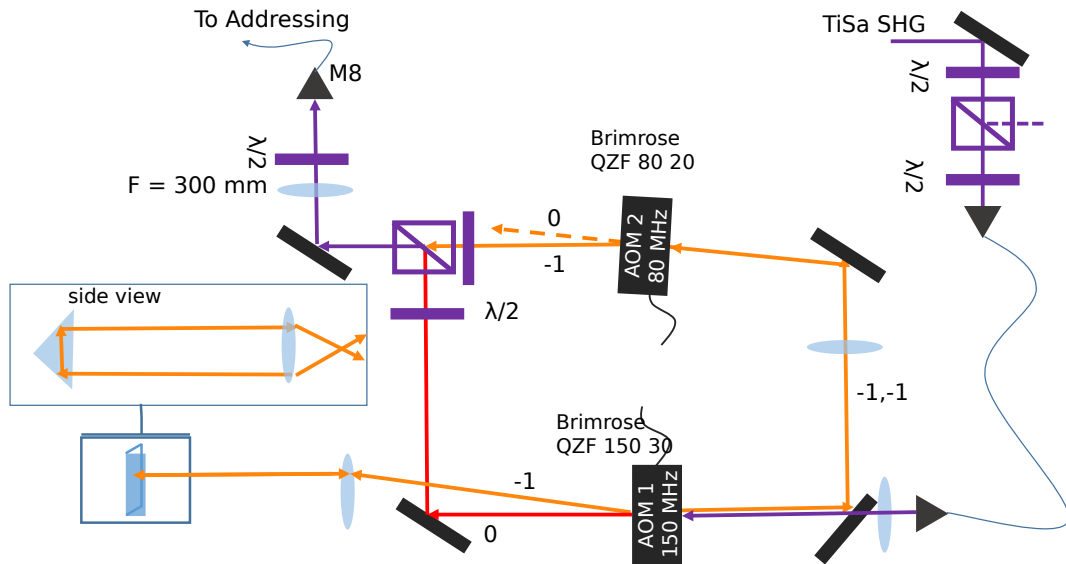


Figure 3.2.1: 393 nm laser optical setup before installing addressing. Two paths are present: a resonant path on the $S_{1/2} \rightarrow P_{3/2}$ transition (in red), and a detuned path (in orange) where a double pass AOM introduces -300 MHz shift, and a single pass AOM an additional -80 MHz. Paths are overlapped on a beam splitter and coupled to a fiber. Numbers on the paths indicate diffraction order, above the AOM's, model, central frequencies and bandwidths are displayed. Lenses in the setup focus the waist of the beam in the AOM's aperture avoiding unwanted beam steering and therefore losing coupling to the fiber. Setup built by V. Krutianskii, image made by him and adapted for this thesis.

The laser used to drive the Raman transition is 393 nm. This light is obtained from a titanium-sapphire laser from MSquared. The laser is optically pumped with 8 W of light at 532 nm coming from a Lighthouse Photonics Sprout laser. The Ti:Sa crystal is contained in a cavity in a bow tie configuration, together with an optical diode, etalon, birefringent mirror, and tunable cavity mirror for frequency tuning and stabilization. The laser can be frequency locked to a wavemeter or to an external cavity.

The fundamental mode is at 786 nm with tunability ranging from 725 nm to 875 nm that can be controlled remotely on the computer. The fundamental light is frequency doubled to 393 nm via a MSquared ECD-X external cavity resonant doubler accessory module. Blue light can be obtained with up to 1 W of power. Before reaching the ion trap, 393 nm light is sent through the setup in figure 3.2.1. The laser serves different purposes, in this thesis it has been used for qubit manipulation as described in section 2.5.1, and for photon generation, section 2.5.2. Therefore for flexibility, the setup contains two paths: a resonant with the $S_{1/2} \rightarrow P_{3/2}$ transition, which goes directly to the ion; and a second path, where the light is detuned by -380 MHz, ideal for exciting the Raman transition described in section 2.2.3.

The introduction of an AOD in the addressing setup further shifts the light by -125 MHz, as we want to work around -400 MHz to excite the Raman transition, this setup had to

be altered. AOM 2 was switched from -1 order to +1 order, and driving frequencies were changed to 180 MHz for AOM 1 and 70 MHz for AOM 2.

3.3 Experiment control

Complex trapped-ion experiments require control over a large network of AOM's and other devices. Furthermore, precise control over laser phase is also fundamental in some experiments. The need of fast and coherent pulse control is fulfilled by an electronic system that can be controlled with a software on a computer where every device connected to the network can be controlled. The experiment control network is sketched in figure 3.3.1. The main components are:

- A computer: from here the experiment is controlled with TrICS (Trapped Ion Control Software)⁴.
- Bus system⁵: parallel communication system between the computer and various electronics such as Direct Digital Synthesizers (DDS).
- Pulse box: it contains a FPGA and DDSs, it receives experiment sequences from the computer and generates accordingly coherent pulses for the experiment electronics.

The computer is connected to the Bus system with a NIDAQ card. DDS used to generate radio frequency signal for AOMs are connected to the Bus system through an optocoupler to avoid ground loops. The computer is connected via Ethernet and with a NIDAQ card to the Pulse Box. The card sends and receive trigger signals, while over the ethernet, experiment sequences are uploaded to the Pulse box.

DDSs are used to generate RF signals that drive the AOMs, they set the frequency and the amplitude of the RF pulses. A set of TTL switches, controlled by the Pulse box, sets the length of the pulses generated by the DDSs connected to the Bus system. These DDSs are controlled on the μs timescale, switches instead are down to few nanoseconds timescale. DDSs in the pulse box instead are capable of a stable and controlled phase relationship, and of switching the phase on the sub microsecond timescale. In the experiment of section 5.3.1, Ramsey pulses need to be phase coherent, thus Pulse box DDSs had to be used. Moreover, during an experiment sequence, the parameters of the DDSs inside the pulse box can be varied, in contrast to DDSs on the Bus system whose frequency and amplitude have to be changed outside a sequence.

In a typical experiment, a sequence of pulses is programmed in python on the computer. When the experiment is run, the computer uploads the sequence to the FPGA inside the Pulse Box. Next, the computer updates the DDSs on the Bus with the appropriate values for the experiment, sends a trigger signal to the Pulse Box and the Pulse Box generates and sends all the signals for the sequence. When the experiment is done, the Pulse box sends another trigger back to the computer, which proceeds to prepare for the next measurement point, it updates the values of the Bus DDSs, reuploads the code to the Pulse Box, sends a trigger to start the sequence and the loop is repeated.

⁴A custom software developed internally in the Blatt's group of the University of Innsbruck used for controlling experiments based on trapped ions

⁵Designed in Innsbruck by G. Hendl.

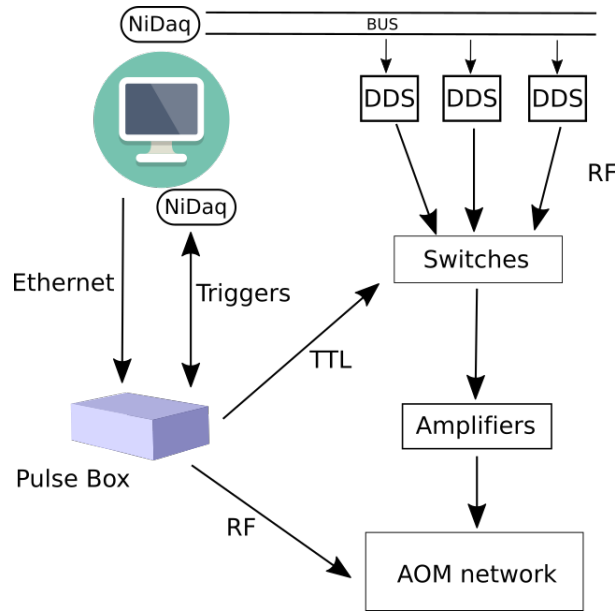


Figure 3.3.1: Schematic of the experimental control. Everything is controlled remotely by a pc. During a sequence a pulse box generates coherent pulses to the appropriate devices.



Figure 3.3.2: Home developed TrICS software. In the figure we can see (A) Experimental device control, from here the user can add new devices and change its parameters, e.g. DDS frequency, switch ON/OFF, attenuation (B) PMT count histograms (C) Experiment scan control, from here experiment sequences can be launched (D) Various plots from camera signal (E) Transition tab to store and modify information about ion transitions.

Chapter 4

Design and simulation of the addressing setup

The purpose of this thesis work was to develop a single-ion-addressed laser system for the purpose of generating single photons and for single ion-qubit control. In this chapter we discuss the design and the implementation of such setup. The design is a crucial part of the work, since there are several requirements that have to be met in order to achieve the proper needed functionalities. In the first section, the requirements are presented together with an overview of the design idea. In the setup an objective was already present, and the choice of an AOD was already made, in anticipation of my project. Hence, we discuss these components as given. The rest of the setup was simulated with the software Zemax, which was used to find the optimal optical components and their placement.

4.1 Addressing system overview and requirements

Single-ion addressing laser systems have already been developed and employed in experiments successfully. The main idea is to focus a laser beam tighter than ion-ion separation and steer it between different ions on a few micro-second timescale. In Innsbruck calcium ions have been addressed in this way, where the steering was achieved with an AOD [?]; At Duke university, laser beams have also been steered with micro-electromechanical systems (MEMS) mirrors [?]. Another idea is to send a normal beam illuminating all the ions, but hiding those who are not addressed. This was done with Ytterbium atoms where by means of a inhomogeneous magnetic field the transition frequencies were shifted shielding selected ions [?].

Our choice was to implement the approach of Innsbruck with an AOD and improve it. The advantage of AODs is to have a switching time in the order of μs , that is used for fast switching between ions. A problem with the implementation of [?] is limited addressing range as the beam clips on the edge of optics when working with strings of ten ions or more at typical confinement. Furthermore, their system is developed for 729 nm light, while our goal is excite the 393 nm transition, this requires new simulations and different optics. Therefore, the new designed system aims to exploit the full capabilities of the AOD while maintaining a very tight focus. In order to achieve this, there are two aspects

to keep in mind: the focus spot, and the addressing range. However the priority was the focus spot as experiments planned in our team involve only a handful of ions in the foreseeable future.

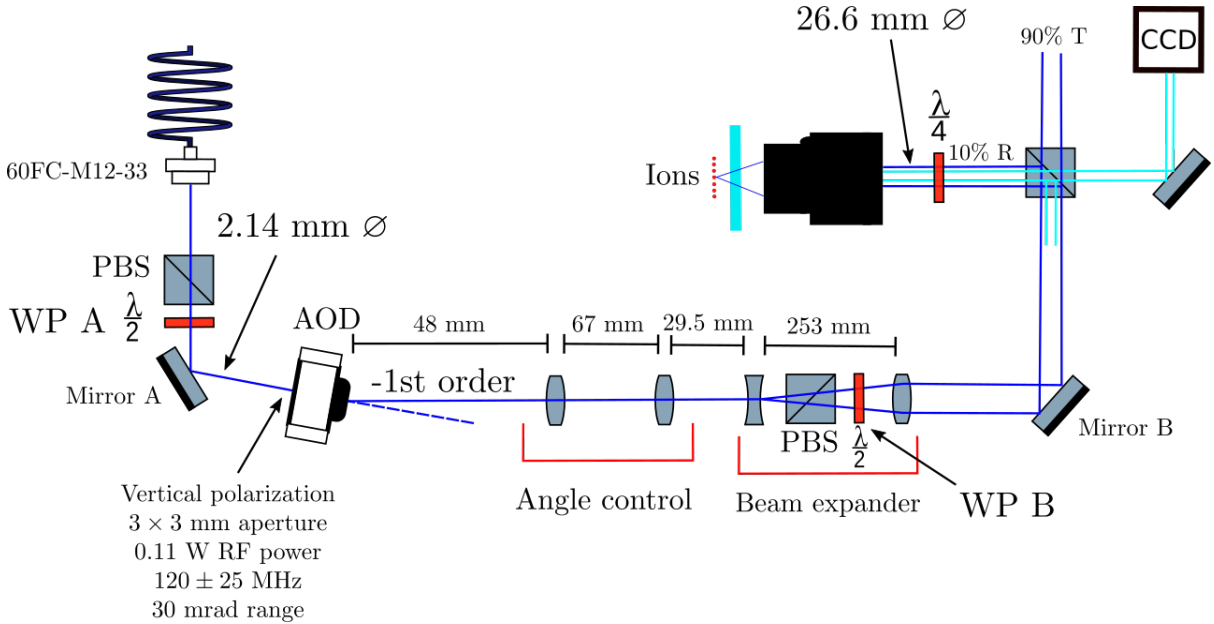


Figure 4.1.1: Scheme of the setup. Light comes from a fiber, polarization is cleaned, and then sent thorough the AOD from Gooch & Housego 4120-3. -1st order diffracted light is refocused into a beam expander, where the beam is broadened before being focused by the objective. All lenses are from Thorlabs, models are from left to right: LA-1059, LA-1131, LA-4252, LA1725; all of them are AR coated for 393 nm. Critical distances between lenses are in the figure, distance between last lens and objective is 722 mm. The 90:10 Beam splitter is custom made by Laser Components GmbH. Diameters \varnothing are expressed as $1/e^2$ of intensity. Between objective and ions there is a 6 mm thick glass of the viewport, as the objective is out of vacuum. $\lambda/2$ waveplates are labeled as WP A, and WP B for future reference. Light blue lines represents 397 nm light coming from the ions into the imaging setup.

The addressing setup should be able to address single ions in a string in order to generate single photons out of single ions via the already discussed Raman process. Ion separations, in the case of two $^{40}\text{Ca}^+$, has been derived in section 2.3.2, for a axial center of mass frequency of 1 MHz is $5.6 \mu\text{m}$. The setup must therefore be able to focus a laser beam down to $1\text{-}2 \mu\text{m}$ waist to essentially eliminate cross talk. As seen in section 2.4.1, a tighter focus can obtained with a shorter wavelength, a bigger lens, or with a shorter focal length. The focusing lens, a.k.a the objective, is shared with the imaging setup, and thus it is given, the focal length is therefore a constant in the problem, see section 4.2. The wavelength is also a constant, as the Raman process happens at 393 nm. This gives only one possibility left to tighten the focus, i.e. by making the beam as broad as possible at the objective input surface.

Figure 4.1.1 presents the final layout of the addressing setup. Some key aspects are now discussed. Beam expansion is achieved with a Galilean telescope, it takes two lenses to form such Telescope, a concave lens to diverge a collimated beam and a convex lens to collimate the diverging beam. The combination of these two lenses takes a collimated

beam and expand it to another collimated beam with an expansion factor of 23.9¹. This expansion part is one of the two essential parts of the addressing setup. The other part is related to the addressing spatial range. Not only, we want to focus the beam to a single ion, but we want to move the beam as well, such that it focuses on a different ion. Therefore, there is a requirement also on the range that can be addressed. This depends on the number of ions and their spacing, we chose to aim to address many tens of ions, this requires the ability to move the focus along the ion string by 150-200 μm . Beam steering is possible with the use of an AOD, the detailed working principle of this device has been discussed in section 2.4.2. Basically the angle of the output beam of the AOD changes as the driving frequency changes. However, the AOD must be placed far behind the objective to leave space for the beam expander, this implies a need to control and redirect the angle of the AOD's output beam to send it to the beam expander and later in the objective without any clipping. This task is accomplished with a pair of converging lenses (Angle control in figure 4.1.1), they refocus the collimated beam into the beam expander, beam then becomes wider, reaches the objective and it is focused on the ion. It is important to get the right lenses at the right distances, the objective has 5 different lenses inside, see section 4.2. The objective was not designed to focus incoming collimated blue light onto the ions, but rather to image photons from the ions onto a camera 1.5 m away from the objective. Simulations showed that a slightly diverging 393nm beam ($\sim 0.5^\circ$), incoming into the objective, will be focused onto the ions. As such, we set the telescope to expand the beam without collimating it, leaving it diverging, so that the objective can focus it at the right position.

The setup displayed in figure 4.1.1 also contains polarization optics. As discussed in section 2.2.3, Zeeman transitions are polarization sensitive, thus polarization control is required. The AOD is polarization sensitive, which means it requires a certain input polarization and outputs another particular polarization, that is the reason why half wave plate are before and after, and additional quarter wave plate is inserted before the objective to obtain circular polarized light. This placement means having a bigger plate than standard, but if placed before in the optical path, the mirror and the beam splitter could alter the polarization. Moreover, the quarter wave plate is zeroth order and custom made, in order to have a greater polarization stability.

The choice of using a 90:10 beam splitter (figure 4.1.1) to overlap the incoming 393 nm addressing laser with the outgoing 397 nm ion fluorescence for imaging is unusual, a common choice is to use a dichroic mirror. However, the light in the imaging path is 397 nm, very close to the 393 nm light of the addressing setup. This would have meant using a very narrow dichroic, the alternative was to use a 90:10 beam splitter, where 90% of the light is transmitted and only 10% of the light is reflected. In this way, only 10% of imaging light is lost, at cost of 90% of addressing laser light, which is not a problem as power is available. Furthermore, this light is focused so tightly that even a small amount of light can excite the ions. On the other end, it is not so straightforward to get more scattered light from the ions, so 397 nm light and the imaging setup must be as efficient as possible, with 10% of losses, ions are still visible on the camera.

¹Since the beam is not collimated after the beam expander, the expansion factor has been calculated as the ratio of the incoming and outgoing beam diameters of the beam expander.

4.2 Objective and AOD

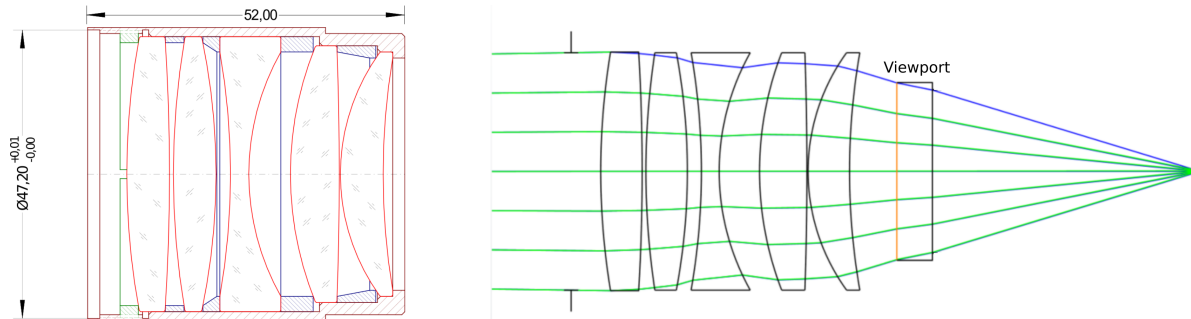


Figure 4.2.1: On the left, section of the custom objective made by Sill Optics, in red the 5 lenses are depicted, while the rest is the mechanical housing, given dimensions are in mm. On the right, Zemax simulation of the objective, viewport is also included.

The objective used to focus the light was already present in the system and had to be taken as it is. It is a custom objective by Sill optics placed outside vacuum, in figure 4.2.1 depiction of the objective and Zemax simulation are present.

This objective has different purposes, it was designed keeping in mind: imaging of ions by collecting 397 nm photons from ions, and imaging them onto a spot 1.5 meters away from the chamber; single-ion focusing with 729 nm light. Every lens is AR coated, the numerical aperture is $NA = 0.289$, thus effective focal length $f = 66.8$ mm. Furthermore, the objective was also designed to take into consideration the fact that it is placed out of vacuum, the light after the objective has to go through a 6 mm fused silica viewport and a further 38.6 mm of vacuum before reaching the ions. The objective is also mounted on a 3 dimensional translational stage to allow for imaging and addressing calibration.

The AOD is from Gooch & Housego, model 4120-3, the datasheet is in Appendix A. All the following parameters are specified in the datasheet, measured values are found in section 5.1. The crystal is Tellurium dioxide (TeO_2), the company specifies a central frequency of 120 MHz, with 50 MHz, bandwidth, so the driving frequency ranges from 95 to 145 MHz with a maximum RF power of 0.3 W. Addressing spatial range of 30 mrad, i.e. angle of deflection $\pm 0.86^\circ$. In this bandwidth the diffraction efficiency should remain above 75 % and have an average of 83 %, further 3% of light is lost due to insertion losses. The active aperture measures 3×3 mm, and the polarization has to be horizontal when entering the AOD, while the specified output polarization is vertical.

4.3 Design simulation

The setup in figure 4.1.1 has been simulated with the software Zemax². The simulation had the purpose of assessing the performance of the setup, i.e. checking the viability of the setup and see if it meets all requirements. It was also used to find suitable lenses for building the setup and their optimal locations. The simulation included: the four lenses, the objective, and the viewport. As there is no option to simulate an AOD, it was not taken in consideration, instead the simulation started at the output of the AOD as

²Zemax OpticStudio is a commercial software based on ray tracing used for designing optical system.

described below. Mirrors and beam splitters were not included in the simulation as their imperfections are not currently known.

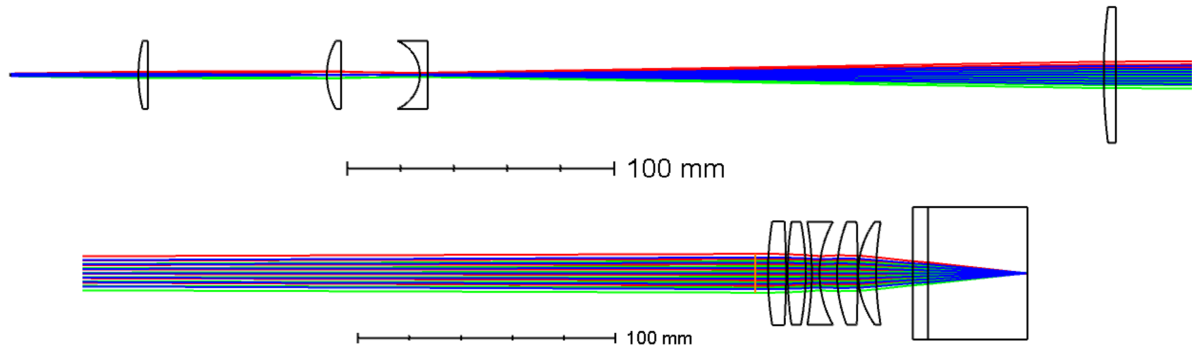


Figure 4.3.1: Zemax simulation of the setup. Rays propagate from left to right starting from top right. Simulation layout has been separated in two for displaying purposes. In the top part, the four lenses are depicted, the rays continue in the bottom part where the objective and image plane are located. Different colors indicate different beams emerging from the AOD at different angles, rays with the same color belong to the same beam. The blue one is the central beam emerging from the AOD with a 0° angle, the red and the green beams emerge respectively with $\pm 0.86^\circ$.

The simulation starts by specifying the input fields, these represent the physical light beam. To account for the ability to change the output angle from the AOD, three different fields have been simulated. One is along the optical axis, while the other two are angled corresponding to the extrema of the AOD bandwidth, so $\pm 0.86^\circ$. Therefore the propagation of these beams represents three different situations of beam direction and should also give an idea of the behavior in between the extrema. Next, the four lenses of the setup were inserted in Zemax, initially with variable radius, thickness and separations. Initial positions and lens focuses were set according to geometrical boundaries given by physical constraints on the optical table where the setup had to be built. The Zemax file of the objective came from the company which designed it and was simply imported in the project. After the objective the 6 mm viewport glass was included and then vacuum for 38.6 mm, which is the distance between the outer facet of the glass and the ion axis. The image plane was therefore set here. The distance between the objective and the viewport was unknown, as it could not be measured. However, this distance was inferred from a Zemax simulation of the imaging path, knowing that the ions focus on the camera 1.5 m away, we determined a space between the viewport and the objective of 14.22 mm. The simulation was carried out with the tool Physical Optics Propagation (POP). POP works by propagating a wavefront represented by an array of discrete points. The array is propagated through every optical component and free space. This method can be used to simulate coherent Gaussian beams with high precision as well as wave phenomena such as diffraction and aberrations. The initial value given to the propagator was the waist of the collimated beam out of the AOD. Since the beam going to the AOD comes from a fiber collimator, the value specified was taken from the datasheet of the fiber collimator, namely Scäfter + Kirchhoff 60FC-M12-33 [?]. Therefore, the specified waist was 1.07 mm.

The first step of the simulation work was to find the appropriate lenses to build the setup.

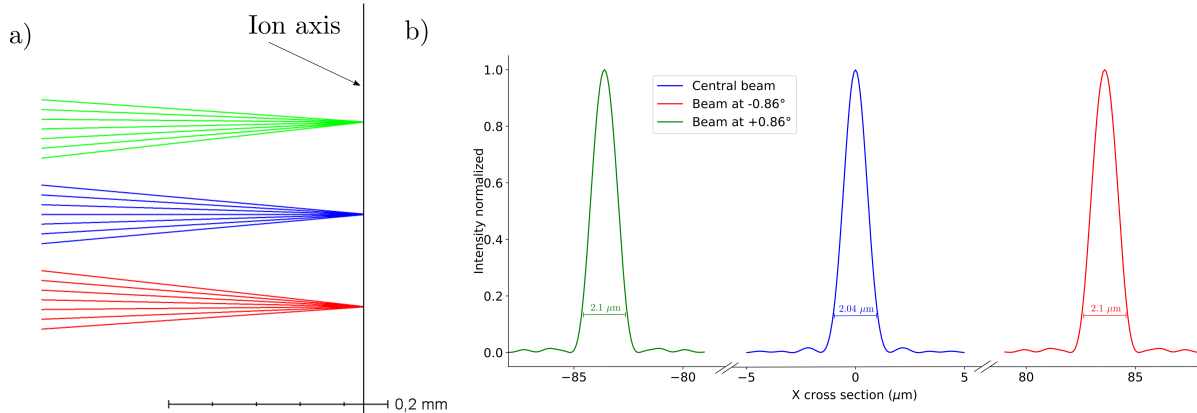


Figure 4.3.2: Zemax simulation at the image plane, where the ions are. a) Addressing range from Zemax simulation, the three beams emerge from the AOD at different angles. The full addressing range here displayed is 168 μm . b) Physical Optics Propagation of the three Gaussian beams with angles of 0, $\pm 0.86^\circ$, and waist at AOD of 1.07 mm. Displayed is the x cross section at the ion axis. Beam diameters (13.5%) are also displayed, the central beam at 2.04 μm is slightly narrower with respect to the outer ones 2.1 μm .

The thicknesses and the radii were optimized trying to achieve the smallest focus spot while maintaining the desired addressing range. The lenses were found with the Zemax tool *Stock Lens Matching*. Basically, the tool compares the simulated lenses with those in a catalogue from different companies and finds the closest match. We opted to rely on the provider Thorlabs, so the search was limited to this company. Found lenses were in order from left to right LA-1059, LA-1131, LA-4252, and LA-1725 and can be seen in figure 4.3.1. Once the desired lenses were found, their Zemax files provided by the company were imported in the project and further optimization was carried on.

The second step was to optimize the lenses position always trying to keep the focus spot as small as possible, and the desired addressing rage of 150-200 μm . This was done using the optimizing tools of Zemax and the merit function. The software can perform multivariate analysis and minimize the focus spot depending on all the assigned variables, which in this case were the distances between the lenses. The final results can be seen in figure 4.3.2, the addressing range is 168 μm set by the bandwidth of the AOD from the specification sheet, while the waist of the central beam is 1.02 μm , beams at the border of the addressing range are 3% broader, with a waist of 1.05 μm .

Another important parameter for the performance of the setup is the addressing error. Qualitatively speaking, in the case of the beam focused on one ion, the addressing error is the leaking light on the neighbour ions. It can be a problem in the case of aberrations that produce bumps on the side of the main Gaussian peak. Especially in the case of diffraction limited system, the profile of the beam is a sinc function that can have more local maxima around the central peak. To estimate the addressing error in a simulation, two ions are placed next to each other at 5.6 μm , and the respective addressing beams have been simulated. The addressing error is different for different physical process, in the case of AC Stark shift, as the experiment discussed in 2.5.1, the shift is proportional to the intensity, so the addressing error is calculated as $I_1(x_2)/I_1(x_1) \simeq 10^{-4}$, where I_1 is the intensity profile of the beam focused on ion 1, and x_1, x_2 are respectively the position of ion 1 and ion 2. In the case of the cavity mediated Raman process, as in the experiment discussed in section 2.5.2, the strength of the process is proportional to the Rabi frequency,

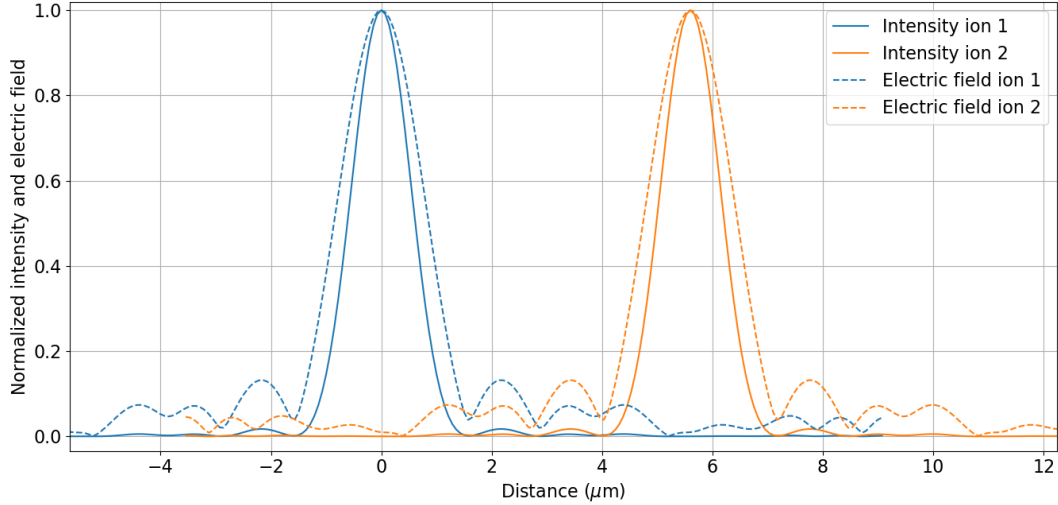


Figure 4.3.3: Beam focused in two different places separated by $5.6 \mu\text{m}$ corresponding to the theoretical equilibrium positions of two ions with axial center of mass frequency of 1 MHz. Addressing error for AC Stark shift is calculated as the ratio of intensities at ion positions: $I_1(x_2)/I_1(x_1) \simeq 10^{-4}$. For Raman transition, the ratio of electric fields is taken: $\sqrt{I_1(x_2)/I_1(x_1)} \simeq 10^{-2}$.

i.e. the electric field. Therefore, the addressing error is given as $\sqrt{I_1(x_2)/I_1(x_1)} \simeq 10^{-2}$. Another aspect that was simulated is the beam profile inside the trap. Optical access to the trap is limited and a tightly focused beam also has a large divergence, which could lead to clipping on the trap's blades or compensation electrodes, scattering light all around the trap. In figure 4.3.4 the top view of the trap is plotted, here we included the three pairs of compensation electrodes, the RF blades, and the cavity mirrors. The blue line represents the radius $W(z)$ from equation 2.4.4 of the addressing beam in the case of a waist W_0 of $1 \mu\text{m}$. To determine the fraction of power lost due to clipping on the compensation electrodes, we can calculate the transmitted power through the top electrodes:

$$P_t = \int_{-\infty}^{\infty} dy \int_{-x_c/2}^{x_c/2} dx P(z), \quad (4.3.1)$$

where $P(z)$ is the power of the Gaussian beam, and x_c is the horizontal position of the compensation electrode. The integral can be computed numerically at position z of the electrodes. The result is plotted in figure 4.3.4, where the lost power $1 - P_t$ is plotted as a function of the waist W_0 . At the expected waist of $1.02 \mu\text{m}$, the power lost is less than 1%, i.e. for 2 μW AOD input power, after considering all the losses in the setup, it means losing less than a nW. The previous calculation holds only if the beam is perpendicular to the x direction so it is important to align it carefully.

To conclude this section, we discuss some aspects of the design. Waist and addressing range were the two key aspects while simulating the design. In the last stage of the simulation, the distances between the lenses were optimized, and their position is a compromise between waist and addressing range, it is theoretically possible therefore to sacrifice one to improve the other. We found that the addressing range can be broadened by moving the beam expander closer to the objective, simulations yielded an addressing range of $180 \mu\text{m}$ for a distance between objective and lens LA-1725 of 622 mm, in this

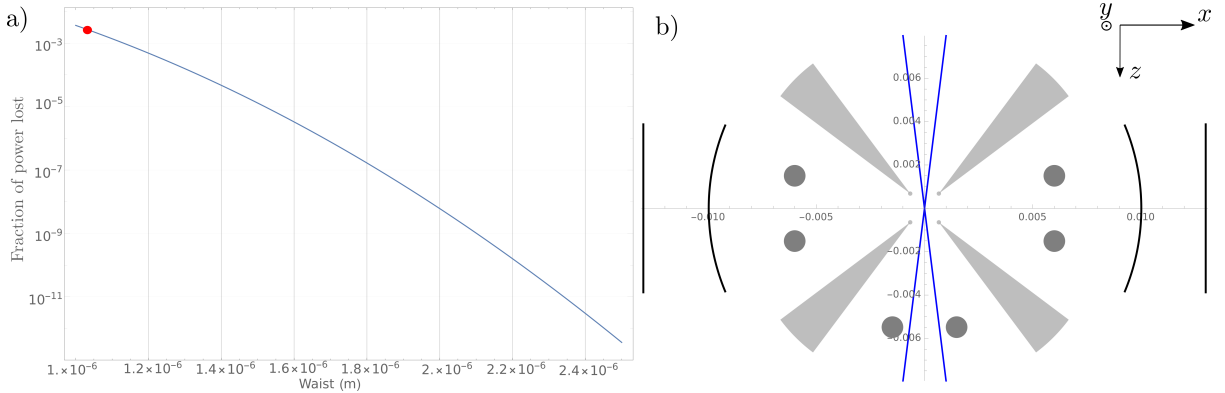


Figure 4.3.4: a) Fraction of power lost due to clipping on the compensation electrodes as a function of the beam waist when focused on ion. Red point represents the waist $1.02 \mu\text{m}$, obtained from the simulation. b) Top view of the trap and addressing beam. Grey circles are the compensation electrodes, blue is the radius $1/e^2$ of the beam focused on the ions with waist of $1.02 \mu\text{m}$, while the black arches represent the mirrors of the cavity. All units are in meters.

case the distance between this lens and the diverging one is 262 mm to keep the focus at the same position. In this configuration a greater addressing range is achieved, but the waist at the ions is $1.1 \mu\text{m}$, broader than the $1.02 \mu\text{m}$ presented in this section. In the simulation, an attempt to decrease addressing range for a smaller waist by moving the beam expander farther away from the objective fails, the addressing range is reduced, but the waist does not significantly change. Moreover in this case, the aberrations, already noticeable in figure 4.3.3, get worse, the small bumps on the side of the main peak increase in height. This could suggest that the system is diffraction limited, the bumps are in fact attributable to a Airy pattern commonly associated with diffraction limited system [?].

4.4 Physical implementation

Once the simulation gave satisfactory results, a test setup was built. The idea of building first a test setup on a different optical table from the main experiment was to check if the system was working as intended, and asses its performance. Due to physical access problems, in the final system there is no space to place a beam profiler, or a polarimeter, and after the objective there is no access to the vacuum and the trap. While on another table everything could be checked and tested. The results of the measurements obtained on this test setup are presented in chapter 5.

Afterwards, the system was moved and implemented on the experiment optical table. For the initial alignment, a counter propagating red beam was sent in the opposite direction: starting from the front of the chamber, through the ions, and through to the objective and back through the addressing path. Since the lenses of the addressing are antireflection coated for 393 nm, the reflection of the red beam was visible and it was possible to align the components such that the beam passed approximately through the center and perpendicular to the surfaces. Calibration was also done with ions and the beam position was indirectly observed on the camera. A string of ion was used as a probe by constantly imaging the ions with 397 nm and 393 nm light on the camera. The 393 nm laser drives the transition $S_{1/2} \rightarrow P_{3/2}$, from $P_{3/2}$ the electron has two other decay channels, $D_{3/2}$,

and $D_{5/2}$, which means that the electron will eventually end up in one of these two states if only the 393 nm and the 397 nm lasers are used. Repumping with 854 nm and 866 nm light the transitions $D_{5/2} \rightarrow P_{3/2}$, and $D_{3/2} \rightarrow P_{1/2}$ avoids this problem and brings the electron back to the fluorescence cycle. To observe where the 393 nm beam is, it is possible to send pulses of 854 nm light such that, when the 854 nm light is off, the ions addressed by the 393 nm laser become dark after decaying from $P_{3/2} \rightarrow D_{5/2}$. The ions become bright again when a new pulse of 854 nm light is sent, therefore if the pulse rate is slow enough it is possible to see the addressed ions as blinking. This allowed to visualize the position and roughly the dimension of the 393 nm beam for the final calibration.

A photo of the installed system is in figure 4.4.1. Here, the collimating lens is mounted on a 3D manual screw-gauge translation stage for fine tuning calibration position of the focus w.r.t. the ion string. Manual screws were later replaced with remote controlled ones from Newport, model PZA12 so that beam alignment is possible without opening the mu-metal enclosure. An iris is also used to block the zeroth order beam from the AOD. Moreover, The AOD is placed on a rotational mount that allows to tilt it in two directions. One direction was used to find the Bragg angle of the AOD to achieve maximum diffraction efficiency, and the other can be used to tilt the axis over which the AOD sweeps. This can be used to compensate for an ion string which is not exactly parallel to the AOD sweeping direction.

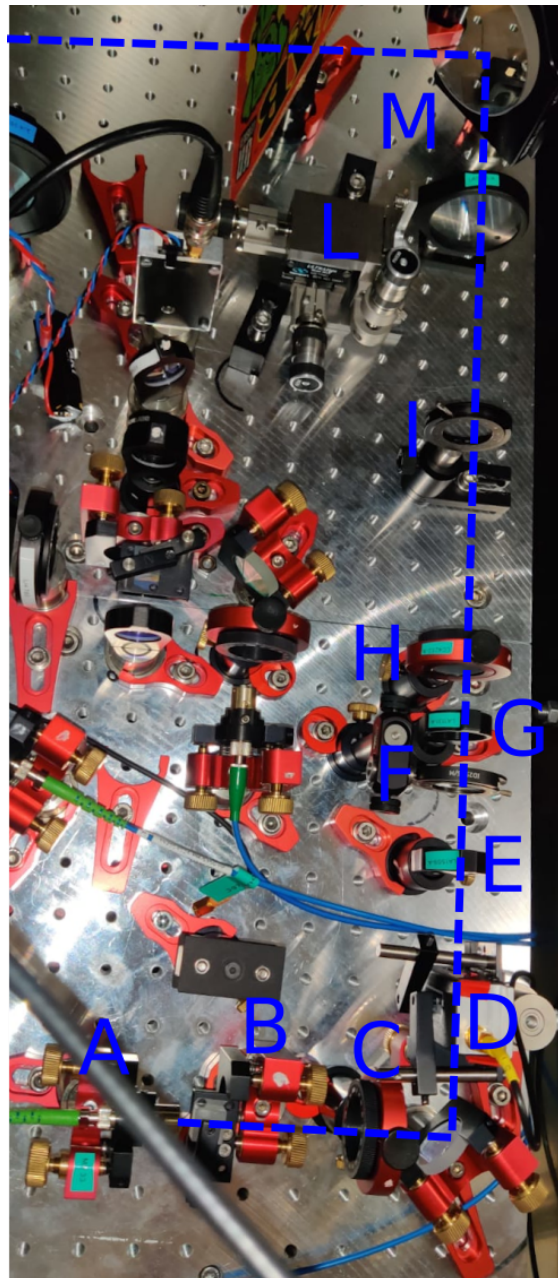


Figure 4.4.1: Photo of the final setup. The blue dashed line is the beam path starting from bottom left at the fiber collimator, all the way to the top where a mirror deflects the beam and send it to the beam splitter. The following elements are visible: (A) Fiber collimator 60FC-M12-33 (B) Polarizing beam splitter (C) $\lambda/2$ (D) AOD (E) Lens LA-1059 (F) Iris to block 0th order (G) Lens LA-1131 (H) Diverging lens LA-4252 (I) Iris (L) Lens LA-1725 on the 3D manual screw-gauge translation stage (M) Mirror.

Chapter 5

Experimental results

This chapter collects all the experimental results obtained during the thesis:

- Section 5.1 contains the characterization of the AOD.
- In section 5.2 we characterized different parts of the setup in a test assembly. Polarization, stability, and focus spot have been checked. In particular, two methods have been used to measure a μm focus spot: razor blade scans, and small pixel size camera.
- In section 5.3, we performed two experiments with trapped ions: single-qubit manipulation has been demonstrated by performing Ramsey interferometry measurements, which also allowed for a check of addressing performance. Second, a cQED experiment has been carried out, single photons were generated from a single ion in a string, via a cavity-mediated Raman process (Sec. 2.2.3).

5.1 AOD

The AOD is the core element of the setup, it is therefore essential to characterize it. The two main parameters we are interested in are the diffraction efficiency and the response time. For the diffraction efficiency we measured the total output power of the light P_{tot} and then the power of the first diffracted order P_1 . Diffraction efficiency is defined as the ratio between the two

$$\text{DE} = \frac{P_1}{P_{tot}}. \quad (5.1.1)$$

Before measuring the diffraction, the optimal RF power to drive the AOD has been found. This was done by maximizing the power of the first diffracted order with the AOD set at its central frequency. Power measurements of the light were done with a Thorlabs PM100D, and the AOD was driven with an amplifier and a RF signal generator. The optimal RF power was found to be 0.11 W, and for the rest of the measurements it was kept at that value. Furthermore, to optimize the linear input polarization, a PBS followed by a half-waveplate were placed before the AOD, the waveplate was rotated trying to maximize the power of the diffracted light. In figure 5.1.1 the plot of the diffraction efficiency as a function of the RF frequency is displayed. Within a bandwidth of 50 MHz from 105 MHz to 155 MHz, we can see that more than 70 % of the light is in the first

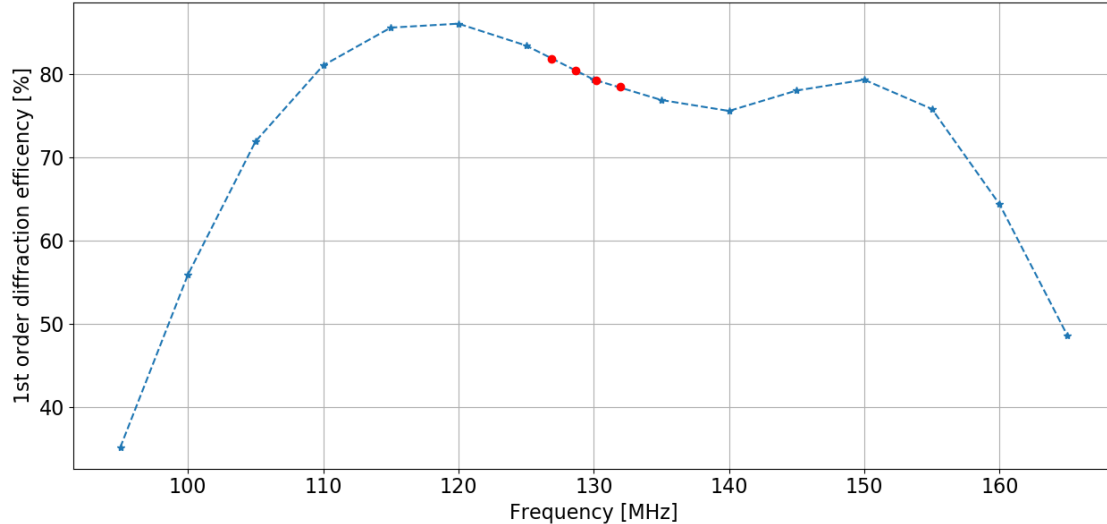


Figure 5.1.1: Diffraction efficiency of the AOD as a function of the RF driving frequency. Red points indicate the frequencies associated with 4 ions loaded in the trap with a axial COM frequency of 780 kHz as the experiment in section 2.5.1, the theoretical separations are $5.15 \mu\text{m}$ for the two outer ones, and $4.77 \mu\text{m}$ for the inner ions.

diffracted order as expected from the datasheet (Appendix A), even though the bandwidth looks shifted with respect to the nominal central frequency of 120 MHz.

The response time is the responding time of the light to a RF frequency change. In order to perform this measurement, a voltage controlled oscillator (VCO) was used to generate the RF signal. The VCO was supplied a square wave that alternated between two voltages corresponding to two different frequencies $\sim 96 \rightarrow 127 \text{ MHz}$. The blue light was measured with a photodiode. The photodiode was aligned with the light at one particular frequency, such that when the light moves, the beam would not hit the diode and the signal generated changes. In figure 5.1.2, the signal of the photodiode, together with the supplied VCO signal are plotted. Response time is $\sim 8 \mu\text{s}$, with $3 \mu\text{s}$ delay and $5 \mu\text{s}$ response. From the beam diameter (13.5 %) we expect $3.3 \mu\text{s}$ response time, while the delay indicates that the distance between the piezo and the edge of the beam is 1.95 mm.

5.2 Full test setup characterization

The test setup was built on an optical table with a spare objective since the one installed in the vacuum chamber was already in use for ion imaging. The layout of the system in figure 4.1.1 was replicated.

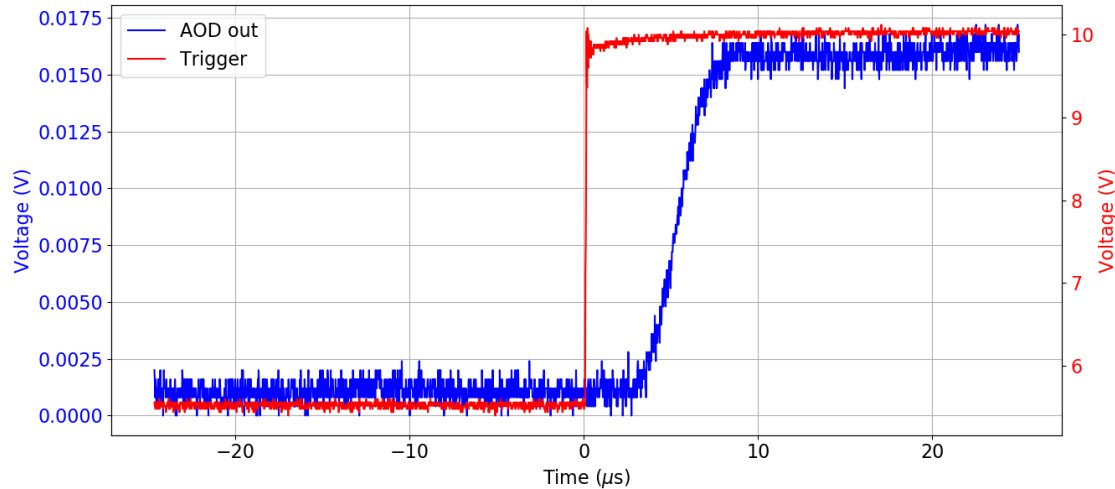


Figure 5.1.2: Response time of the AOD, plotted are the photodiode signal in blue on the left y axis, and the VCO voltage is in red on the right axis. The voltage of the VCO determines the frequency of the RF sent to the AOD. The change here corresponds to a frequency shift of ~ 31 MHz.

5.2.1 Waist: Knife-Edge method

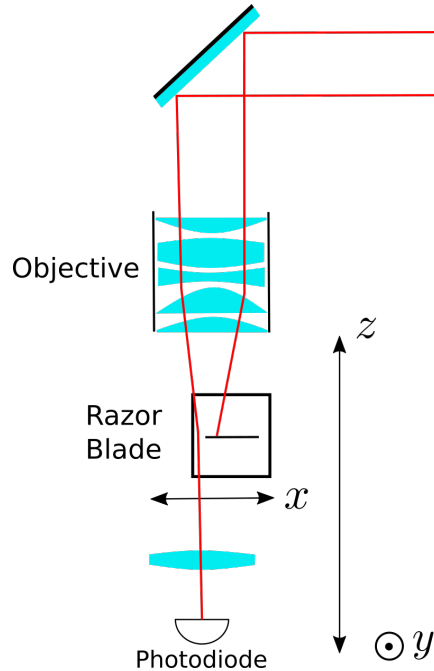


Figure 5.2.1: Scheme of the razor scan. A translation stage allows for moving the blade in the direction x , perpendicular to the beam, and z , along the beam.

Measuring a micrometer scale waist is not an easy task, the first method applied consisted of mounting a razor blade on a translational stage. The setup used is showed in figure 5.2.1, after the objective the blade is present, and since the beam is quickly diverging after the focus, a lens is used to refocus the light into a photodiode. The stage is moved in the x direction cutting the beam perpendicularly such that the blade is scanning the beam

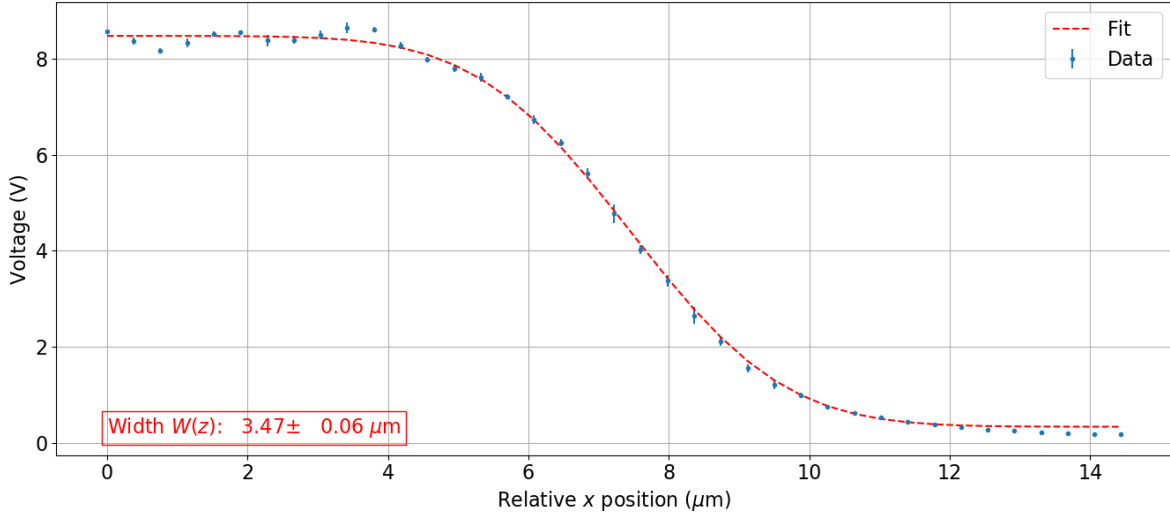


Figure 5.2.2: Razor scan at the waist of the beam $z = 0$

profile. A filter was inserted in order to not saturate the photodiode. In the z direction the stage was controlled with a manual screw with resolution of $1\text{ }\mu\text{m}$. While in the x direction, the stage had to be moved with sub-micrometer precision, so instead there was a piezo actuator controlled by custom software. The same software also controlled a multimeter that measured the voltage of the photodiode. To get the profile $W(z)$ (equation (2.4.4)) of the beam, the measurement procedure was as follow

- Position blade at desired z coordinate
- Scan beam in x direction with blade
- Beam width extrapolation
- Shift z direction

The procedure is repeated for sufficient values of z to scan at least few Rayleigh ranges. The beam width can be calculated from the scans by fitting the data with equation (2) of [?]. In figure 5.2.2 we report an example of a scan taken at the waist of the beam. The errorbars come from statistical average, every data point is a mean over 5 measurements, and the error is the standard deviation. The fit in this case gave a width W of $3.47 \pm 0.06\text{ }\mu\text{m}$, the smallest width obtained with this method. It is broader than $1\text{ }\mu\text{m}$ simulated waist. Furthermore, the profile $W(z)$ was not symmetric and could not be fitted with equation (2.4.4). A possible explanation is that this method is not suitable for measuring micrometer waists with a typically commercially-available razor blade, the accuracy is limited by the positioner and the blade roughness. The latter was not known at the few micrometer scale of the beam waist. In comparison, authors of [?] have used, instead of a common razor blade, a glass substrate etched with an effective knife-edge features with which they were able to measure a $1\text{ }\mu\text{m}$ waist.

5.2.2 Waist: Camera

Since the Knife-Edge method was not particularly effective, a more direct approach has been subsequently adopted. We measured directly the beam with a camera from IDS

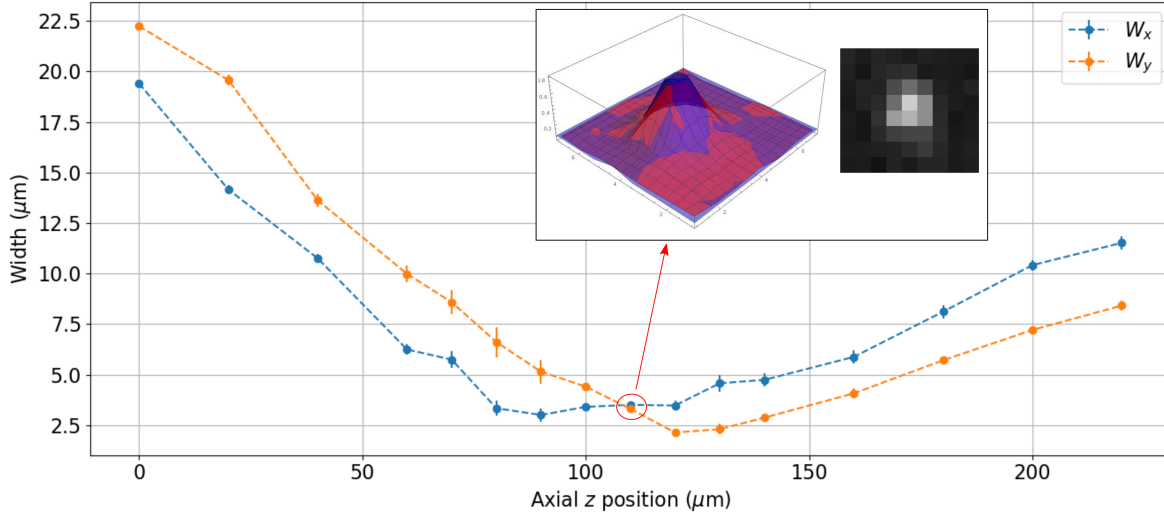


Figure 5.2.3: Profile of the Gaussian beam along z measured with the camera. Errorbars are estimated from fit. In the inset an example of raw data and Gaussian fit. In red color, the normalized pixel value is displayed, while the blue curve is a fitted 2D Gaussian. On the axis there is the pixel number.

model UI-1490LE-M-GL. This particular camera has a pixel size of $1.67 \mu\text{m}$. It should therefore be suitable to measure a focus spot with a μm precision. A $1 \mu\text{m}$ focus should hit one single pixel, and if aligned between two pixels, a Gaussian profile could also be fitted. In addition, unlike the Knife-Edge technique, a camera provides 2-dimensional information about the beam shape and can be exploited to look for aberrations in the system. The setup is almost the same as figure 5.2.1, but the camera now replaces the razor blade, and there is no need for scanning in the x direction, as the z is enough to reconstruct the profile $W(z)$. An additional filter was used to optimize the light reaching the camera in order to not saturate it and get a visible signal. For every desired z displacement, a photo with the camera is taken, post processed, and then the camera is displaced to the new z coordinate. Post processing is done by fitting the pixel values with a 2-dimensional Gaussian

$$P = A \exp \left\{ -\frac{(x - x_0)^2}{2\sigma_x^2} \right\} \exp \left\{ -\frac{(y - y_0)^2}{2\sigma_y^2} \right\}. \quad (5.2.1)$$

The fit parameters are A , x_0 , y_0 , σ_x , and σ_y . From the standard deviations σ_x and σ_y the beam width in the x and y direction at position z : $W_x(z)$, $W_y(z)$ can be determined as $W_x(z) = 2 \cdot 1.67 \cdot \sigma_x$ and respectively $W_y(z) = 2 \cdot 1.67 \cdot \sigma_y$, where $1.67 \mu\text{m}$ is the pixel size (see caption of figure 2.4.1). The full profiles $W_x(z)$ and $W_y(z)$ can be found in figure 5.2.3. Here anomalies can be noticed. The profile is asymmetric and does not follow equation 2.4.4, nonetheless a width $< 2.5 \mu\text{m}$ has been measured. We decided to install the system and measure more accurately the waist with a single ion.

5.2.3 Polarization

As discussed in the design section 4.1 and in the Raman process 2.2.3, polarization is an important component as atomic transitions are polarization sensitive, thus the polarization capabilities of the system had to be tested. The goal is to achieve vertical, horizontal,

Polarization	$\lambda/2$ WP B (°)	$\lambda/4$ (°)
Horizontal	267.2 ± 0.1	49.7 ± 0.1
Vertical	312.5 ± 0.1	48.1 ± 0.1
Right circular	267.2 ± 0.1	4 ± 0.1
Right circular	312.5 ± 0.1	93.1 ± 0.1
Left circular	267.2 ± 0.1	95.4 ± 0.1
Left circular	312.5 ± 0.1	3.1 ± 0.1

Table 5.2.1: Polarization at the ion position and angles of the waveplates $\lambda/2$ WP B and $\lambda/4$ (Ref. figure 4.1.1) that set the polarization. Numbers are found as maxima or minima of a sine fit of the polarization data in appendix B.

left circular, and right circular polarization at the ion position and test how well they are achieved. Polarization can be changed with two plates: a half wave plate after the AOD, and a quarter wave plate right before the objective, see figure 4.1.1. In order to characterize the polarization at various points in the optical path of the addressing setup, the three Stokes parameters S_i [?] were measured with a polarimeter from Scäfter + Kirchhoff series SK010PA.

Stokes parameters quantify the type of polarization of an electric field. Linear polarized light has Stokes parameters $S_2, S_3 = 0$, while $S_1 = \pm 1$ for horizontal and vertical polarization respectively. Circular polarized light has $S_1, S_2 = 0$ and $S_3 = \pm 1$ for right hand and left hand circular polarization respectively.

The first step was to characterize the polarization after the $\lambda/2$ WP B (see figure 4.1.1), the main result from this characterization is that horizontal polarization can be achieved immediately after WP B with an angle of $267.2 \pm 0.1^\circ$, and vertical is achieved with an angle of $312.5 \pm 0.1^\circ$ obtained from fitting a sine on the first Stokes parameter. From the same fit, the semiperiod of the polarization is $45.3 \pm 0.6^\circ$ consistent with the 45° expected for a half waveplate.

Afterwards, we measured the polarization after the objective at the focus spot where the ions ideally sit. For this measurement we set the $\lambda/2$ WP B first at 267.2° , and then at $312.5 \pm 0.1^\circ$, for both numbers we measured the three Stokes parameters as a function of the $\lambda/4$ angle. Results are summarized in table 5.2.1, in appendix B the full plots are reported.

5.2.4 Stability

It is imperative to know the stability of the system in terms of polarization and beam pointing. This means knowing over the course of hours or days if the setup needs to be re-optimized or calibrated. First we measured polarization, it was set to be right circular: $\lambda/2$ set to 267° , and $\lambda/4$ set to 4° . We recorded the three Stokes parameters for a total of one hour, this data is plotted in figure 5.2.4. It can be seen that the polarization is stable within short term fluctuations (due to device precision) over a period of one hour.

Beam pointing stability is the stability of the focus position, which could drift in any direction for any reason. To test it, we recorded the position of the focus for a period of one hour with the camera. The camera was positioned at the focus with the same setup discussed in section 5.2.2, and then a video was recorded. The video was later analyzed

by tracking the brightest pixel over time. In figure 5.2.5 we can see the horizontal x and vertical y position of such pixel. In the horizontal direction, fluctuations of one single pixel can be noticed, which could be a result of the light hitting between two pixels. In the vertical direction the fluctuations are in the order of two pixels, this could indicate that the position might have shifted by one entire pixel over this period. This means that the focus position is stable with an upperbound of $1.6 \mu\text{m}/\text{hour}$. We have to consider that this measurement was taken on a open table, a more precise beam pointing stability measurement is carried out with ions in the closed mu-metal shield, see section 5.3.1.

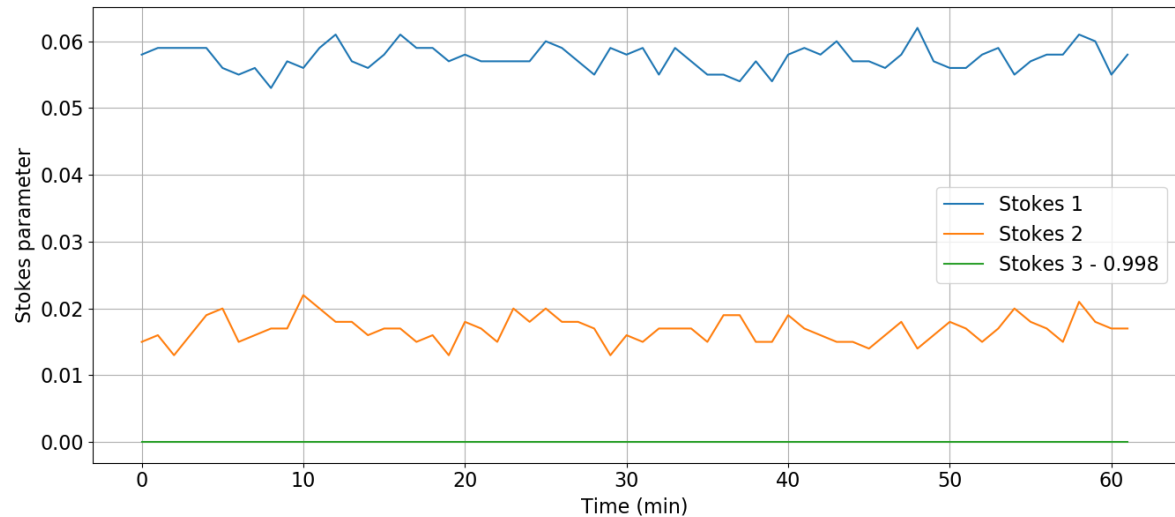


Figure 5.2.4: Right circular polarization stability at the ion position over a period of one hour. To the third parameter S_3 , 0.998 has been subtracted.

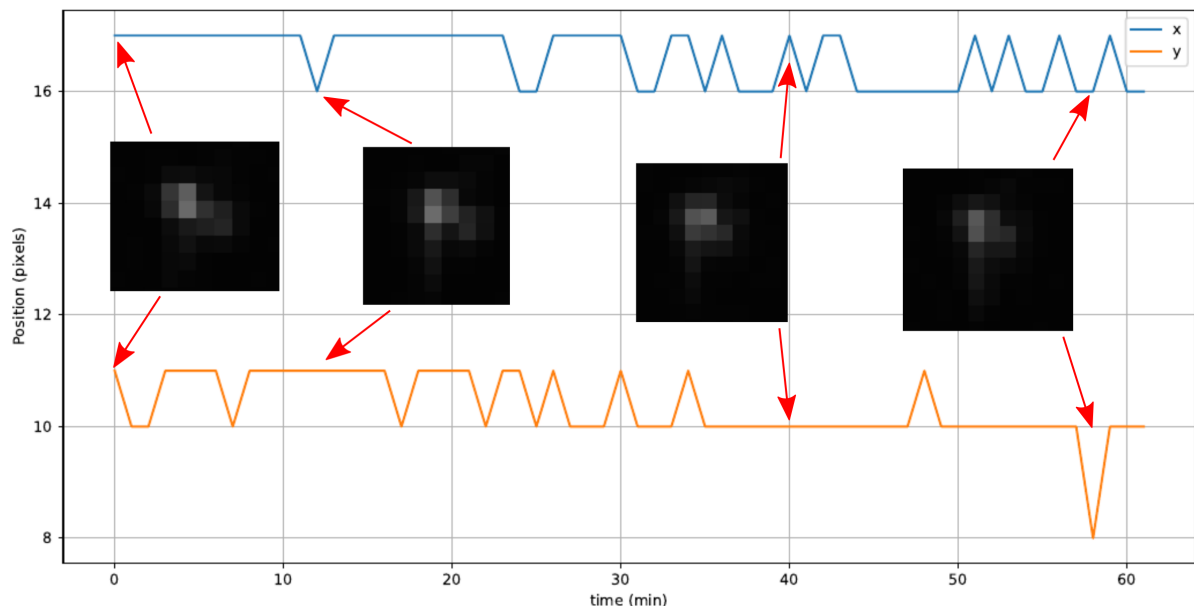


Figure 5.2.5: Beam pointing stability at the focus position over a period of one hour. The 2 lines represent the horizontal x and vertical y position of the beam in unit of pixels. In the insets, some examples of raw data are given.

5.3 Final installed system

After the tests presented in the previous sections, the setup was installed next to the ion chamber and focused on the ions as described in section 4.4. As there is no more physical access to the focus spot, more advanced quantum optics experiment have to be carried out in order to measure properties of the system, such as focus spot size and addressing error. The first experiment designed aims exactly at measuring these two quantities: a Ramsey experiment was performed on four loaded ions, from which the beam shape due to AC Stark shifts on the ions could be measured. The second experiment involves three ions and the goal was to generate photons via Raman process from one single ion leaving the state of the other two unaltered, demonstrating therefore the new possibility to emit single photons from individual ions in a string.

5.3.1 Single qubit manipulation



Figure 5.3.1: Pulse sequence of the experiment. The sequence is repeated for different AOD frequencies moving the 393 nm beam across the ion string. From the ion excitations, the Rabi frequency of the 393 nm laser can be inferred. The length τ was varying.

The goal of this experiment is to perform the Ramsey experiment discussed in section 2.5.1. In summary, we want to sweep the 393 nm beam along the ions, the sequence in figure 5.3.1 is repeated for different AOD frequencies, and from the ion excitation we can infer the Rabi frequency of the 393 nm laser. Before the actual experiment, some preliminary measurements have to be taken, thus in this section we show first the following:

- Global Rabi flops with 729 nm, from this we can measure the $\pi/2$ pulse time and show individual ion readout with the camera.
- Ramsey fringes without 393 nm, showing coherent control over the ion qubits.
- 393 nm pulse length scan, to get the length τ of the Raman pulse and furthermore to estimate the addressing error.

After these preliminary steps we performed the Ramsey experiment scanning the frequency of the AOD, as we scan, every single ion will produce a signal proportional to the Rabi frequency Ω that can be fitted to obtain the focus spot size.

The experiment was done with four ions loaded in the trap with endcap voltages of 714 V and 700V, for which numerical simulations yield a axial COM frequency of ~ 767 kHz. The 393 nm laser was locked to the wavemeter and detuned by ~ 3 GHz, ref. section 2.5.1. Rabi flops are showed in figure 5.3.2. Some point are missing in the plot due to a melting event of the ion crystal. The system took the data points while ions were melted, therefore they have been removed. Rabi flops are also damped due to residual thermal distribution, since we only perform Doppler cooling, ions are not in the ground state, but rather in a thermal state [?]. The $\pi/2$ time is extrapolated from the first flop as the time it takes

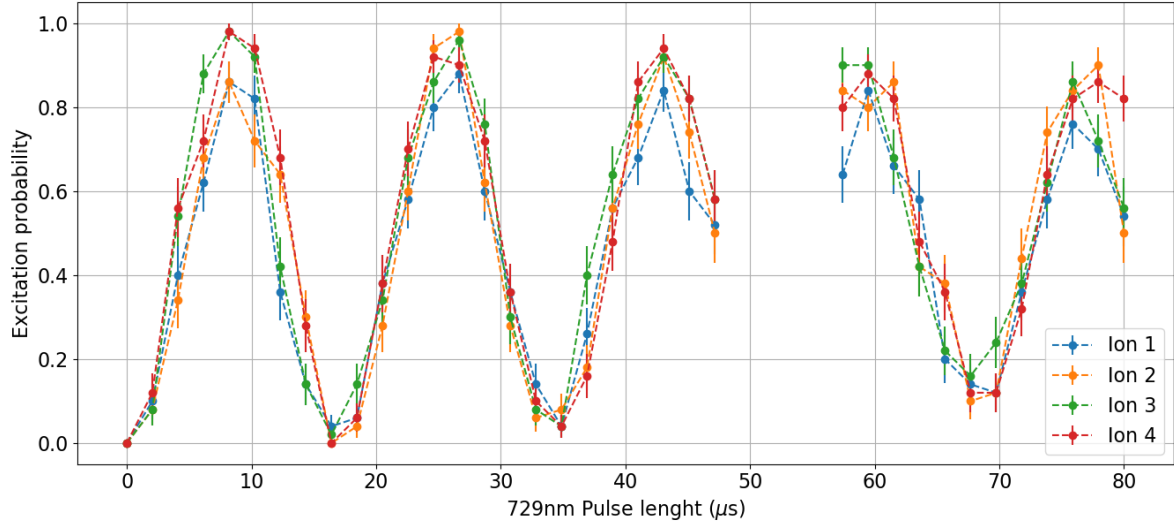


Figure 5.3.2: Global Rabi flops on 4 ions. Errorbars on the excitation probability have been assigned according to the error on estimating the probability of a binomial distribution. Some points were removed due to a melting event.

for the ions to reach excitation probability $P_D = 0.5$, we estimated $4.2 \mu\text{s}$. Errorbars on the excitation probability have been assigned according to the error on estimating the probability of a binomial distribution [?]

$$\sigma = \sqrt{\frac{P_D(1 - P_D)}{N}}, \quad (5.3.1)$$

where $N = 50$ is the number of repetitions. Ramsey fringes without the 393 nm pulse are presented in figure 5.3.3, the $\pi/2$ time was set to $4.2 \mu\text{s}$. The phase ϕ between the two pulses was scanned, and afterwards it was set to $\phi = \pi/2$ for the rest of the experiment.

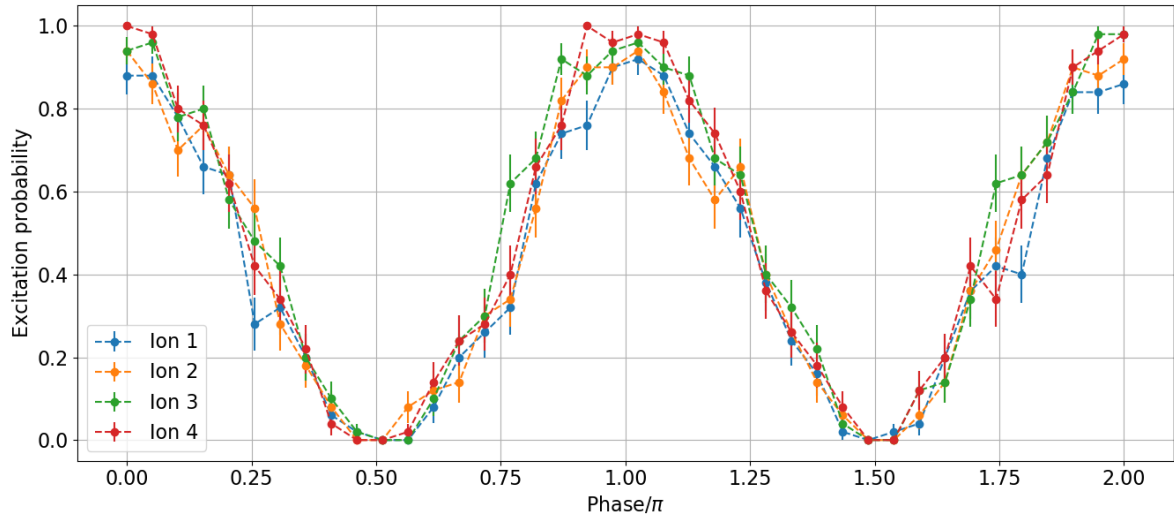


Figure 5.3.3: Ramsey fringes for 4 ions without 393 nm. A $\cos^2(\phi)$ behavior can be noticed showing coherent control of the ion states.

The Raman pulse length τ was chosen in a way that the shift caused by the 393 nm light does not skip any fringe, i.e. the shift induced by the Raman laser does not flip the ion state. To get this timing, τ can be scanned and the appropriate value can be estimated, the plot is in figure 5.3.4. We set τ to be $25 \mu\text{s}$, such that we do not excite the ion more than halfway the fringe.

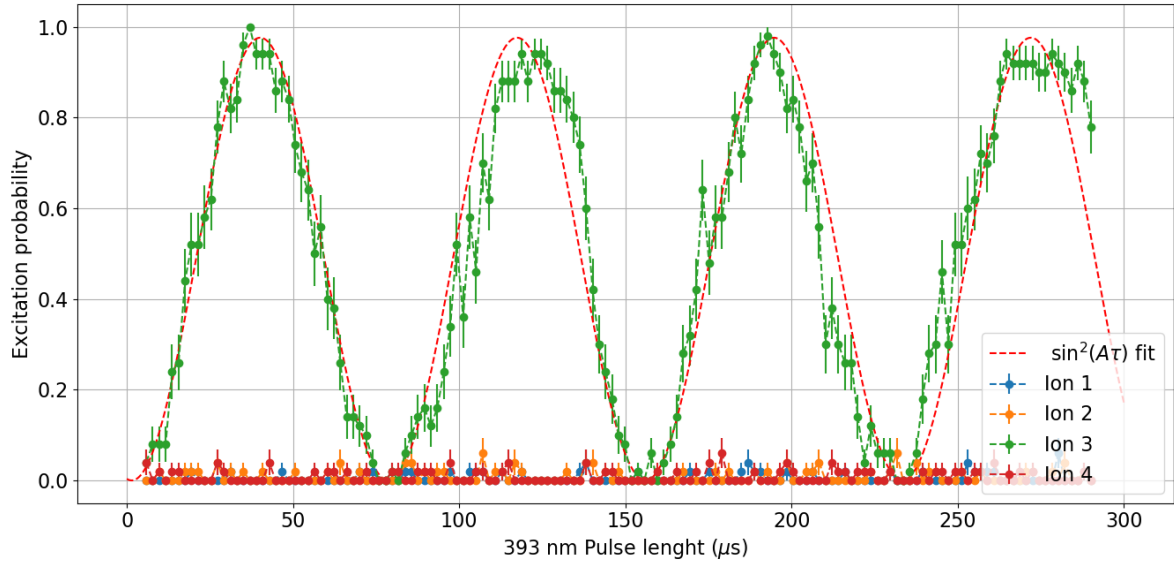


Figure 5.3.4: 393 nm AC Stark flops. The pulse length τ of the 393 nm laser is scanned while shining over one single ion. The red curve is a fit of $\sin^2(A\tau)$, where A is proportional to the Rabi frequency of the laser focused on the third ion.

Having chosen all the parameters, the experiment can now be performed. The AOD frequency is scanned, during this scan the beam is moved from ion to ion and the excitation probability of all ions is measured, this is then translated to Rabi frequency with equation (2.5.4). The result after post analysis can be seen in figure 5.3.5. Specifically, the intensity of the beam has been determined from the probability P_D as discussed, errors are propagated accordingly. To calibrate the beam position scale in micrometers, the axial COM mode (767 kHz) of the trap is measured by performing 729 nm spectroscopy on the carrier and motional sideband. Ions positions can be then numerically calculated (cfr. section 2.3.2). AOD frequencies corresponding to the maxima in figure 5.3.5 are attributed to the ion positions, and corresponding frequency shifts to distances. By comparison, we found a conversion factor of $3.03 \mu\text{m}/\text{MHz}$. The four peaks have been fitted with a Gaussian function to obtain the waist of the beam when focused on the different ions. The waists yielded by the fits are from right to left $\omega_1 = 1.23 \pm 0.20 \mu\text{m}$, $\omega_2 = 1.25 \pm 0.19 \mu\text{m}$, $\omega_3 = 1.35 \pm 0.22 \mu\text{m}$, $\omega_4 = 1.39 \pm 0.20 \mu\text{m}$.

The addressing error can be estimated from the Stark flops in figure 5.3.4. In this measurement, the addressing beam was focused on one ion and the Raman length τ is scanned. This increases the interaction time of the laser with the ions, and if the interaction is long enough even the tail of a Gaussian can induce some excitation on the ions on the side of the one being addressed. In the scan displayed, the pulse reached $300 \mu\text{s}$ and there is no excitation on any ion apart from the one flopping. Others scans went up to $500 \mu\text{s}$, and still no visual excitation is present. While this means that no quantitative number can be determined for the addressing error, an upper bound can still be given. A

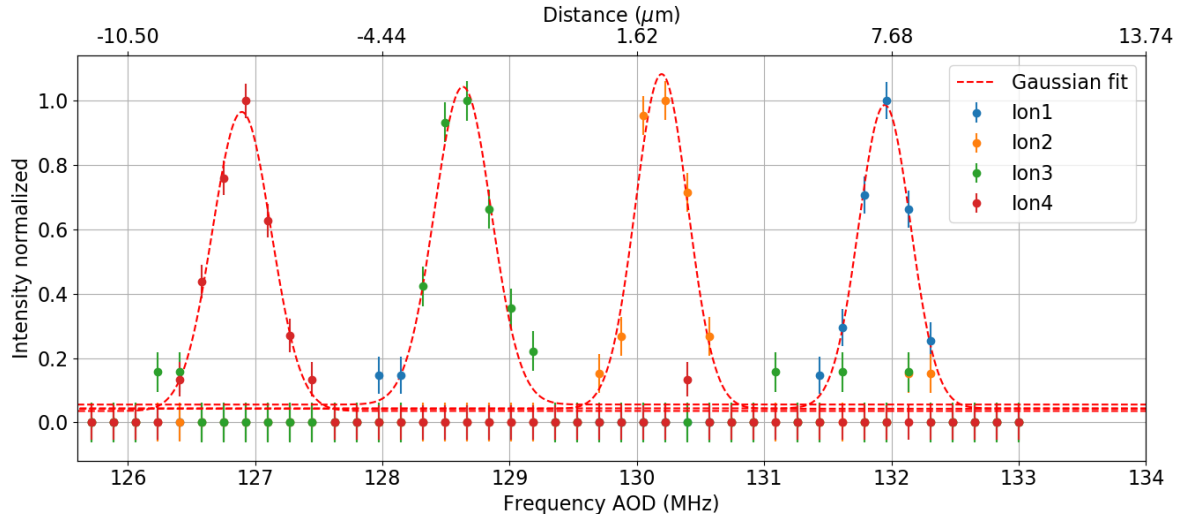


Figure 5.3.5: AOD scanning of four ions via Ramsey interferometry. The normalized intensity comes from the Rabi frequency calculated from the excitation probability P_D using formula (2.5.4). The upper micrometer scale is calibrated by comparing the center of the Gaussian fit with the numerically calculated ion positions.

sinusoidal fit $\sin(A\tau)$ has been done on the data, it is not perfect probably due to intensity fluctuations of the lasers, or magnetic field fluctuations. Nonetheless, from the fit we can determine the Rabi frequency on the third ion as $\Omega_3^2 = 4\Delta \cdot A = 487 \text{ MHz}^2$, see equation (2.5.3). Assuming in the worst case scenario that an excitation on the second ion appears right after $500 \mu\text{s}$, the addressing error should be at most $\Omega_2^2/\Omega_3^2 < 10^{-3}$.

During this experiment we scanned the AOD twice in an interval of 30 minutes to measure the stability of the system. In figure 5.3.6 the peak on the third ion has been overlapped between the two scans. A fit gives the central frequencies of the two peaks, and their difference determines the stability over a period of 30 minutes, we estimated a stability of $0.20 \pm 0.07 \mu\text{m}/\text{h}$.

To conclude this section, we remark that the 393 nm pulse acts as a single qubit gate on individual ions. The Ramsey experiment carried out by scanning the AOD frequency demonstrated the ability of the system to manipulate single qubits fulfilling the first goal of this thesis.

5.3.2 Photon production

The second goal of having an addressed 393 nm setup is to generate single photons from individual ions in a chain which enhances the network ability of our ion-cavity quantum network interface. In this experiment we produced photons from the central ion of a 3-ion string. Photons are produced by a pulse of 393 nm light focused on the central ion of three via the Raman process described in section 2.5.2. In the experiment we scanned the length of this pulse and recorded the integrated photon detection probability, measured leaving the cavity. The generated photon is emitted into the cavity, transmitted through the mirror of the cavity, coupled into an optical fiber, and passes through a PBS before reaching a superconducting nanowire single-photon detector (SNSPD)¹ which clicks if a

¹Scontel SNSPD model FCOPRS-CCR-2TW75+2SW85

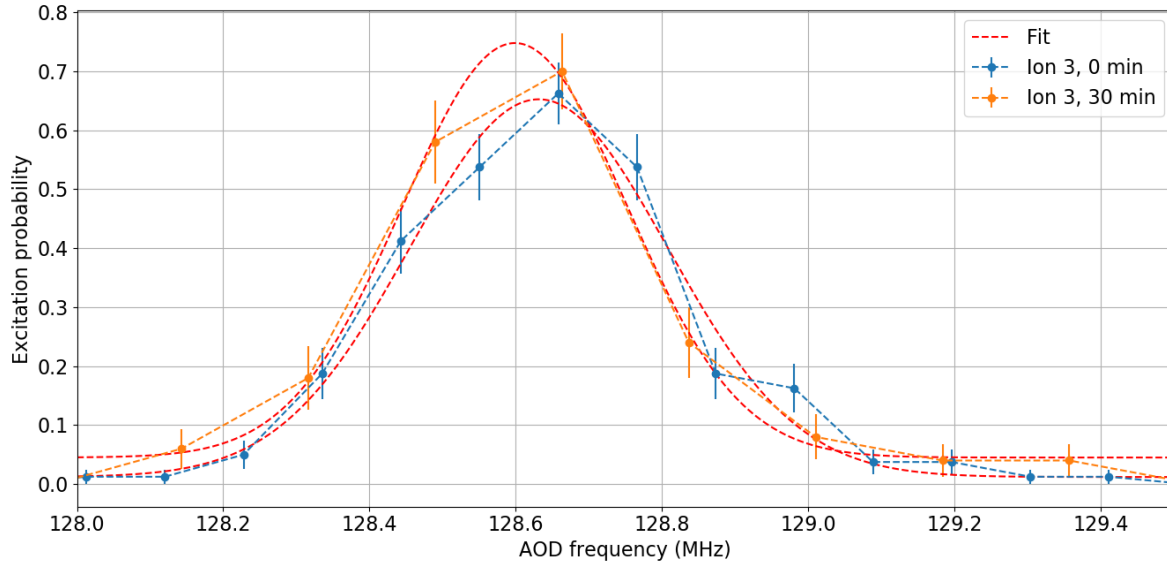


Figure 5.3.6: AOD scanning on one single ion repeated after 30 minutes to measure stability as difference of the center of the two peaks: $0.20 \pm 0.07 \mu\text{m}/\text{h}$. Processing of the data has been done as in figure 5.3.5.

photon is detected. In contrast to the previous experiment, the precise (to the kHz level) frequency of the Raman laser is key to generate cavity photons. Here the laser is locked to an external cavity (ref. [?]). The existing AOM network was established to leave the Raman laser 400 MHz detuned from the S-P transition. To account for the additional 127 MHz detuning of the AOD, we shifted the frequency of two AOMs in the 393 nm setup (see section 3.2).

We loaded three ions in the trap with a axial COM frequency of ~ 820 kHz, which means ion separations of $5.4 \mu\text{m}$, this is enough to be able to place all of the ions near the maxima of the cavity standing electric field². We locked the 393 nm laser to the cavity and scanned the Raman transition with the double pass AOM 1 (ref. figure 3.2.1). The transition chosen is $|S_{1/2}, -\frac{1}{2}\rangle \rightarrow |D_{5/2}, -\frac{5}{2}\rangle$, see details in section 2.2.3. We tried to maximize the photon counts coming from the ions by shifting the cavity along the cavity axis. In the experiment we included an initial stage of Doppler cooling and a final stage of state detection with the camera. Furthermore, the locking light 806 nm in the cavity was switched off during the photon generation process, in this time the cavity maintained its position with a sample and hold. For each Raman pulse length, the experiment is repeated $N = 200$ times to get an estimate for the average photon probability and the ion excitation probability. These two quantities are plotted in figure 5.3.7 and 5.3.8, respectively. Errorbars on the excitation probability are calculated as the previous section, while for the photon probability the error is given by Poissonian statistics [?]

$$\sigma_{ph} = \frac{\sqrt{N_{click}}}{N}, \quad (5.3.2)$$

where N_{click} is the number of times a photon has been detected with respect to the total N repetitions. As we can see, only the addressed ion gets excited as it emits a photon showing that single ion emission was achieved. The probability of getting photon is low

²For a cavity-trap angle of 4.1° we calculated the maxima to be separated by $5.7 \mu\text{m}$.

< 15% compared to other experiments with the same setup, for example [?], however no optimizations were performed to increase it, in the outlook we discuss how to improve it.

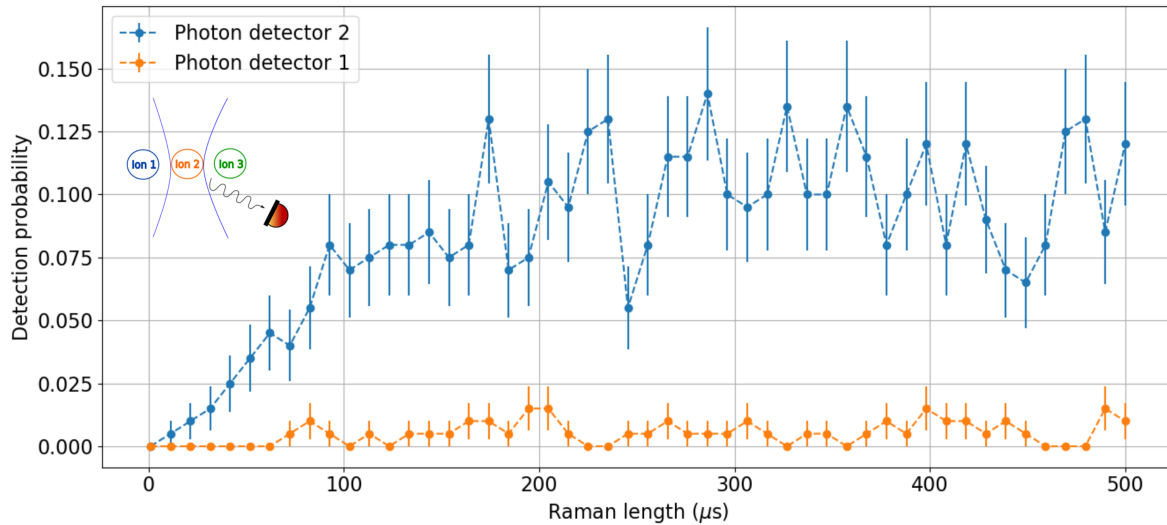


Figure 5.3.7: Measured cavity-photon wavepacket during an addressed cavity-Raman process on the middle of three ions. The two detectors measure the Horizontal (1) and Vertical (2) photons emitted by the ion, in figure 5.3.8 excitations of the ions during the process are plotted. Under the legend a diagram sketching the situation where only the middle ion is addressed and emits photons.

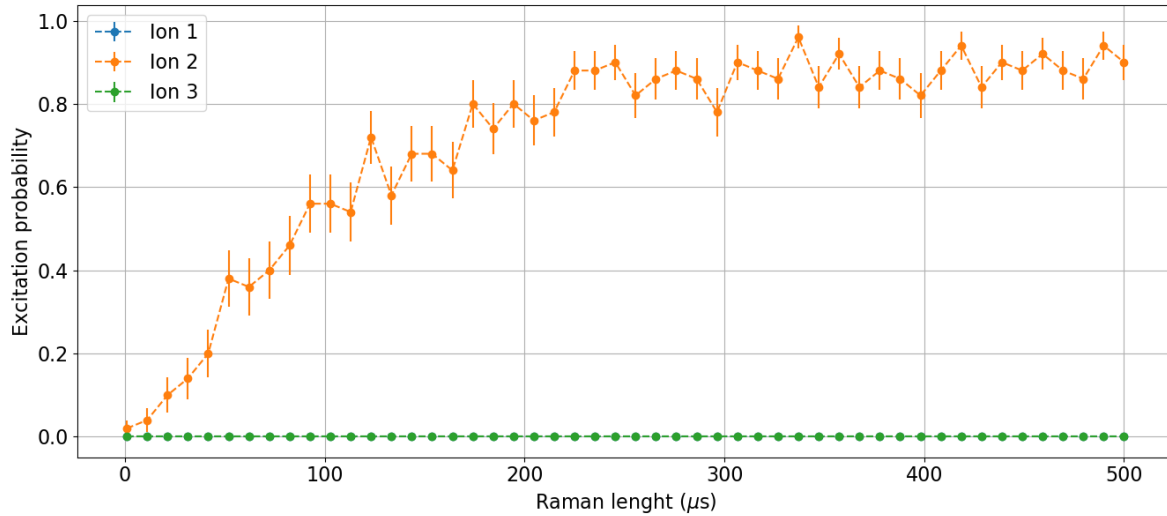


Figure 5.3.8: Qubit state of the ions measured during the same experiment as presented in Figure 5.3.7: cavity photon generation from the central ion using the addressed Raman laser.

Chapter 6

Conclusions and outlook

In this thesis works, an optical setup for single ion focusing of 393 nm laser has been designed and built. The design was based on the already successful addressing setups built in other experiments, but it has been improved to avoid clipping that limited the addressing range. The software Zemax was used to simulate, and check the performance of the design. Optimal lenses for the construction were also found with the software. Once the simulation was satisfactory, a test setup was built on an optical table where it has been characterized in terms of performance, polarization capabilities, and stability. Here the smallest waist measured was $2.4 \mu\text{m}$, the switching time of the AOD was in the order of $7\text{--}8 \mu\text{s}$, and addressing range $>150 \mu\text{m}$. Afterwards, the setup was moved and aligned on the ions, where limited physical access did not allow for such easy checks, but instead more advanced quantum optics experiments have been performed.

The setup was intended to be used for single photon generations and single qubit manipulations. Both of the purposes has been fulfilled: the photon generation was demonstrated in the experiment in section 5.3.2, here a string of three ions was loaded into the trap and the focused laser aligned with the central one. A laser pulse triggered the photon generation exclusively from the intended ion. The photon detection probability was $< 15\%$, and can definitely be further improved as particular attention was not given to the polarization, but the system already has the capabilities for precise polarization setting. Permanent magnets are still mounted parallel to the previous Raman laser direction, they can be moved in the new direction to improve photon emission. Qubit manipulation was carried out in the Ramsey interferometer experiment, here we measured the AC stark shift caused by the 393 nm light by imprinting a phase on the qubit encoded in the 729 nm transition. State readout of the qubits showed the different final states for different phases due to the 393 nm light. Moreover, with this experiment the waist of beam was measured to be $1.2 - 1.3 \mu\text{m}$ and the addressing error was estimated to have an upper bound of 10^{-3} .

The next natural step is the generation of photons from different ions currently undergoing at the moment of this thesis writing. Afterwards, entanglement can also be produced between a single ion and a photon, once more stabilization improvement on the setup are done. This project has several future development, on the quantum network side, this work represents an improved interface between network and quantum computer, transmission bandwidth has drastically increased, dedicated qubits for networking, storing, and computation can now be created and manipulated. It also opens up to the possibility to create multi-ion-multi-photon states with applications in quantum metrology.

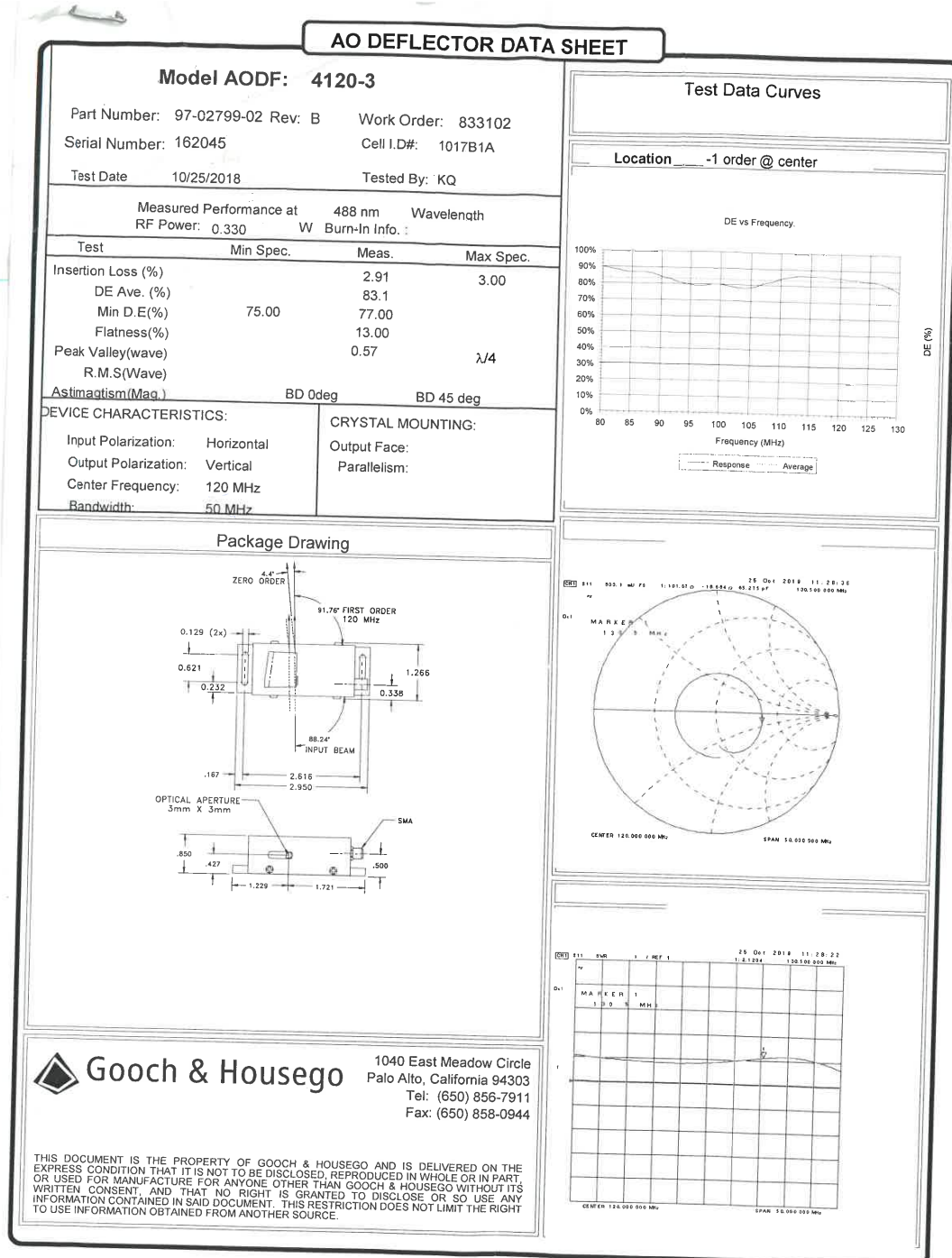
Bibliography

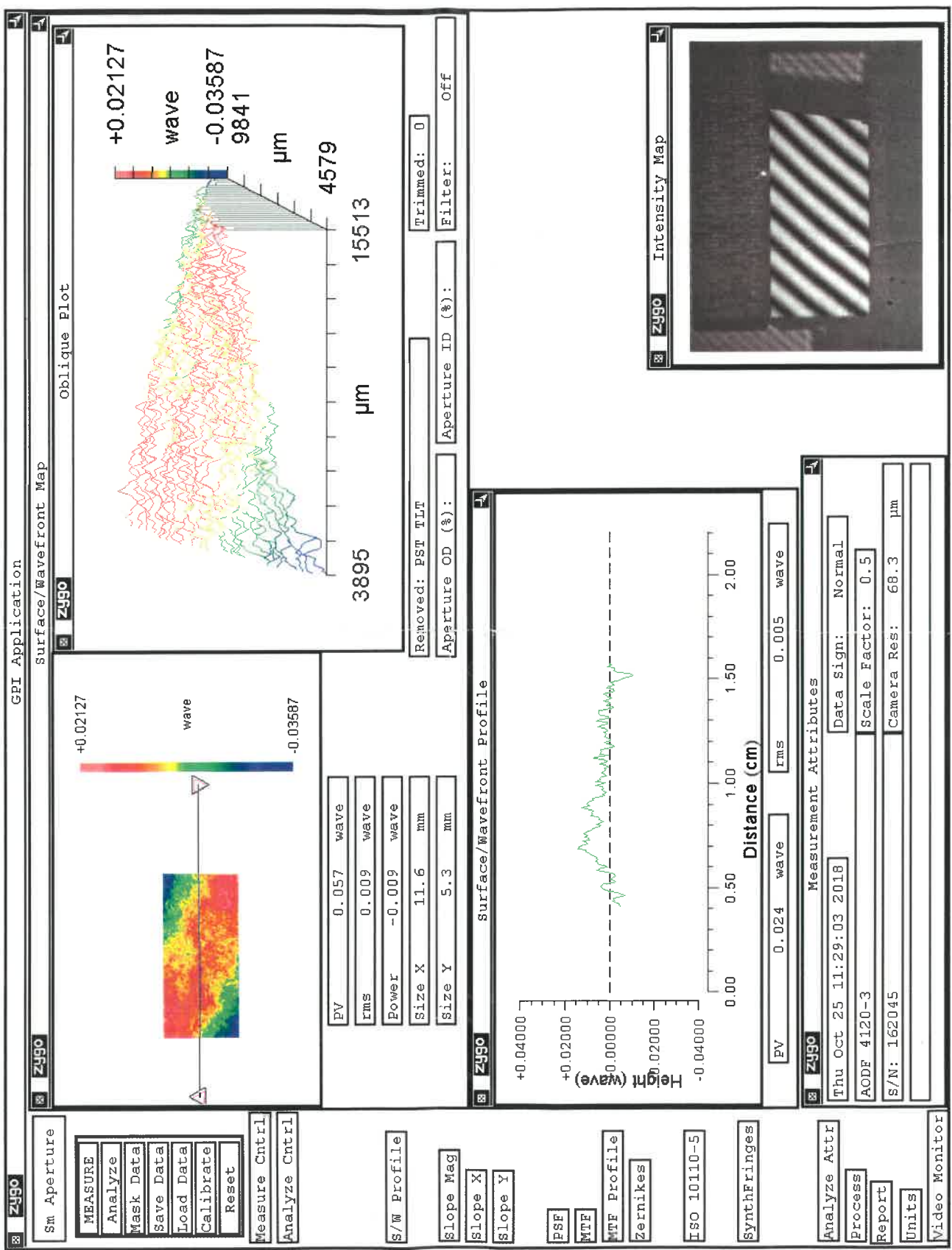
- [1] Antonio Acín, Immanuel Bloch, Harry Buhrman, Tommaso Calarco, Christopher Eichler, Jens Eisert, Daniel Esteve, Nicolas Gisin, Steffen J Glaser, Fedor Jelezko, Stefan Kuhr, Maciej Lewenstein, Max F Riedel, Piet O Schmidt, Rob Thew, Andreas Wallraff, Ian Walmsley, and Frank K Wilhelm. The quantum technologies roadmap: a european community view. *New Journal of Physics*, 20(8):080201, aug 2018.
- [2] Peter W. Shor. Polynomial-time algorithms for prime factorization and discrete logarithms on a quantum computer. *SIAM J. Comput.*, 26(5):1484–1509, oct 1997.
- [3] Lov K. Grover. A fast quantum mechanical algorithm for database search. In *Proceedings of the Twenty-eighth Annual ACM Symposium on Theory of Computing*, STOC ’96, pages 212–219, New York, NY, USA, 1996. ACM.
- [4] I. M. Georgescu, S. Ashhab, and Franco Nori. Quantum simulation. *Rev. Mod. Phys.*, 86:153–185, Mar 2014.
- [5] H. J. Kimble. The quantum internet. *Nature*, 453(7198):1023–1030, jun 2008.
- [6] Stephanie Wehner, David Elkouss, and Ronald Hanson. Quantum internet: A vision for the road ahead. *Science*, 362(6412), 2018.
- [7] *Proceedings of IEEE International Conference on Computers, Systems and Signal Processing*, 1984.
- [8] Ivan B. Damgård, Serge Fehr, Louis Salvail, and Christian Schaffner. Cryptography in the bounded quantum-storage model. In *Proceedings of the 46th Annual IEEE Symposium on Foundations of Computer Science*, FOCS ’05, pages 449–458, Washington, DC, USA, 2005. IEEE Computer Society.
- [9] Joseph F. Fitzsimons. Private quantum computation: an introduction to blind quantum computing and related protocols. *npj Quantum Information*, 3(1), jun 2017.
- [10] P. Kómár, E. M. Kessler, M. Bishof, L. Jiang, A. S. Sørensen, J. Ye, and M. D. Lukin. A quantum network of clocks. *Nature Physics*, 10(8):582–587, jun 2014.
- [11] Daniel Gottesman, Thomas Jennewein, and Sarah Croke. Longer-baseline telescopes using quantum repeaters. *Phys. Rev. Lett.*, 109:070503, Aug 2012.
- [12] Vasil S. Denchev and Gopal Pandurangan. Distributed quantum computing: A new frontier in distributed systems or science fiction? *SIGACT News*, 39(3):77–95, September 2008.
- [13] J. I. Cirac and P. Zoller. Quantum computations with cold trapped ions. *Phys. Rev. Lett.*, 74:4091–4094, May 1995.

- [14] Andreas Stute, Bernardo Casabone, Bernhard Brandstätter, Dr. M. Habicher, H. G. Barros, Piet O. Schmidt, Tracy E. Northup, and Rainer Blatt. Toward an ion–photon quantum interface in an optical cavity. *Applied Physics B*, 107:1145–1157, 2012.
- [15] Isaac L. Chuang Michael A. Nielsen. *Quantum computation and quantum information*. Cambridge Series on Information and the Natural Sciences. Cambridge University Press, 1 edition, 2004.
- [16] H. Häffner, S. Gulde, M. Riebe, G. Lancaster, C. Becher, J. Eschner, F. Schmidt-Kaler, and R. Blatt. Precision measurement and compensation of optical stark shifts for an ion-trap quantum processor. *Phys. Rev. Lett.*, 90:143602, Apr 2003.

Appendix A

AOD datasheet





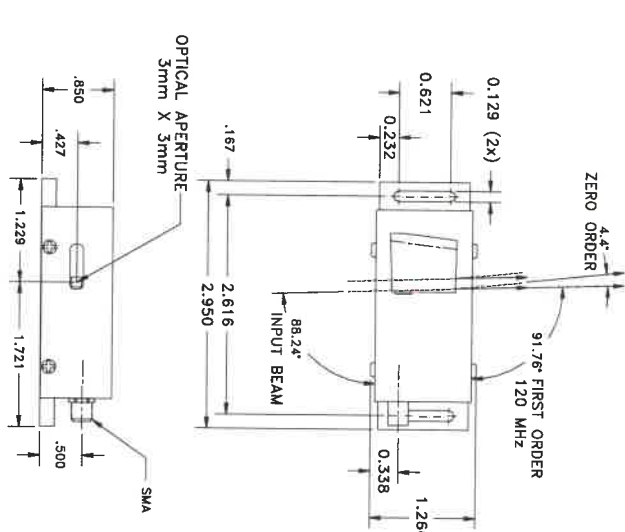
SPECIFICATIONS

AO Medium	TeO ₂
Acoustic Mode	Shear, off axis
Acoustic Velocity	.65 mm/μs
Wavelength	413 nm
Input Polarization	Horizontal
Output Polarization	Vertical
Insertion Loss	3%
Center Frequency (F _c)	120 MHz
RF Bandwidth	50 MHz
RF Power	<0.3 W
Active Aperture	3mm Diameter
Average Diffraction Efficiency	N/A
Flatness Across Bandwidth	N/A
Min Diffraction Efficiency	75%
Peak Valley at 633 nm	λ/4
RMS at 633 nm	N/A
VSWR	2.2:1
Scan Angle	N/A
Time Bandwidth	N/A

Notes:

1. First order @ 120MHz collinear to input +/- 45°
2. Impedance matching frequency range 80-145MHz

OUTLINE DRAWING



Document

09/13/13

Control

THIS DOCUMENT IS THE PROPERTY OF GOOCH & HOUSEGO. IT IS NOT TO BE REPRODUCED OR DISCLOSED IN WHOLE OR IN PART OTHER THAN BY EMPLOYEES OF GOOCH & HOUSEGO AND ITS CONTRACTED REPRESENTATIVES AND DISTRIBUTORS. ANY EXCEPTION REQUIRES THE WRITTEN CONSENT OF AN AUTHORIZED REPRESENTATIVE OF GOOCH & HOUSEGO.

TOLERANCES: XXX ± .01	DR	T. Ng 9/3/2013	Gooch & Housego
MATERIAL:	CHK	DESCRIPTION: AODF 4120-3	
FINISH:	APP	3MM APERTURE	
		PART NUMBER: 97-02799-02	REV. B

Appendix B

Polarization characterization

Here we report the figures for the polarization characterization of section 5.2.3. Every figure contains a fit of a sine function $A \sin(\omega x + \phi)$, where x is the angle of the corresponding waveplate. The fits are used to determine the maxima and minima of the curves which indicates the closest point to the desired polarization, see table 5.2.1 for results.

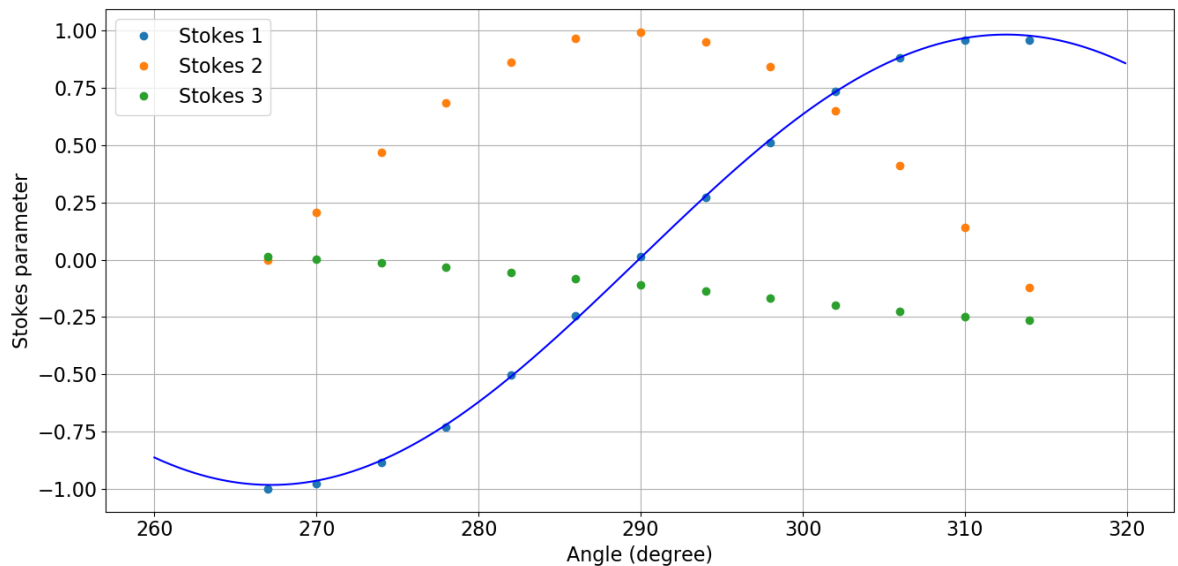


Figure B.0.1: Polarization after the $\lambda/2$ WP (see figure 4.1.1) as a function of the $\lambda/2$ WP B angle. Blue line is a sine function fit: $A = 0.983 \pm 0.007, \pi/\omega = 45.3 \pm 0.6^\circ$.

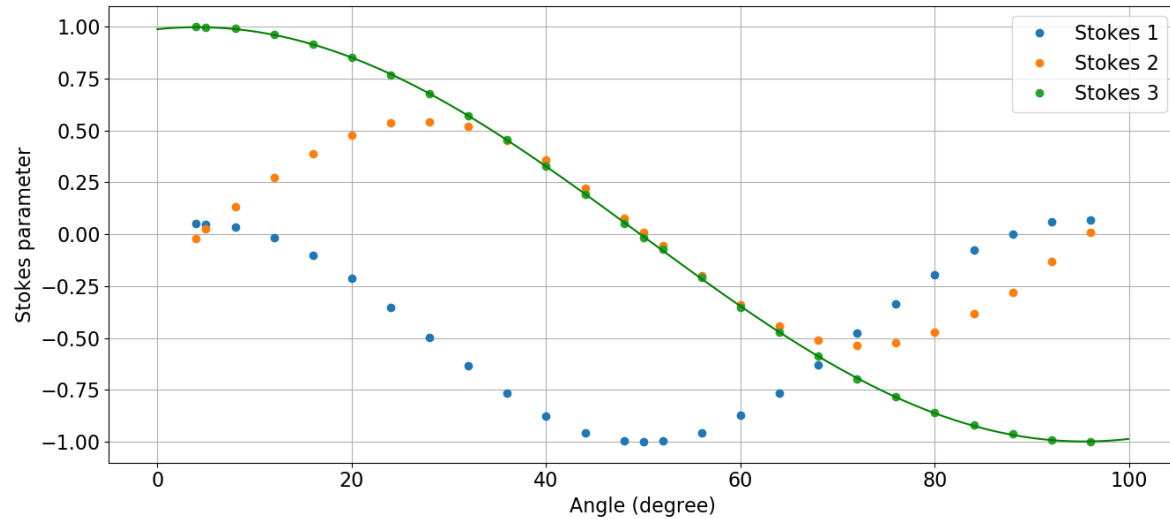


Figure B.0.2: Polarization after the objective at the focus spot as a function of the $\lambda/4$ angle with $\lambda/2$ WP B set to horizontal (267°). Green line is a sine function fit: $A = 0.998 \pm 0.02$, $\pi/\omega = 91.3 \pm 0.3^\circ$.

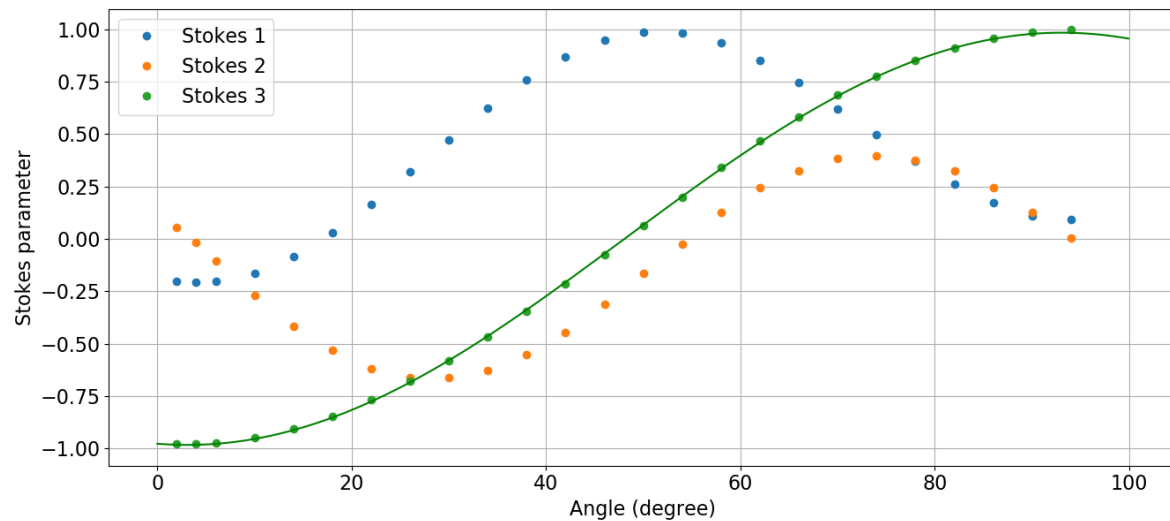


Figure B.0.3: Polarization after the objective at the focus spot as a function of the $\lambda/4$ angle with $\lambda/2$ WP B set to vertical (314°). Green line is a sine function fit: $A = 0.982 \pm 0.003$, $\pi/\omega = 90.0 \pm 0.5^\circ$